Magnetospheric configuration and dynamics of Saturn's magnetosphere: A global MHD simulation

Xianzhe Jia,[1] Kenneth C. Hansen,[1] Tamas I. Gombosi,[1] Margaret G. Kivelson,[1,2] Gabor Tóth,[1] Darren L. DeZeeuw,[1] and Aaron J. Ridley[1]

[1] We investigate the solar wind interaction with Saturn's magnetosphere by using a global magnetohydrodynamic simulation driven by an idealized time-varying solar wind input that includes features of Corotating Interaction Regions typically seen at Saturn. Our model results indicate that the compressibility of Saturn's magnetosphere is intermediate between the Earth's and Jupiter's, and the magnetopause location appears insensitive to the orientation of the interplanetary magnetic field. The modeled dependences of both the magnetopause and bow shock locations on the solar wind dynamic pressure agree reasonably well with those of data-based empirical models. Our model shows that the centrifugal acceleration of mass-loaded flux tubes leads to reconnection on closed field lines forming plasmoids, an intrinsic process ("Vasyliūnas-cycle") in Saturn's magnetosphere taking place independent of the external conditions. In addition, another type of reconnection process involving open flux tubes ("Dungey-cycle") is also seen in our simulation when the external condition is favorable for dayside reconnection. Under such circumstances, plasmoid formation in the tail involves reconnection between open field lines in the lobes, producing stronger global impacts on the magnetosphere and ionosphere compared to that imposed by the Vasyliūnas-cycle directly. Our model also shows that large-scale tail reconnection may be induced by compressions driven by interplanetary shocks. In our simulation, large-scale tail reconnection and plasmoid formation take place in a quasi-periodic manner but the recurrence rate tends to be higher as the dynamic pressure becomes higher. While large-scale plasmoid release clearly is an important process in controlling the magnetospheric dynamics, it appears insufficient to account for all the losses of plasma added by the magnetospheric sources. We find that a large fraction of the planetary plasma is lost through the magnetotail near the flanks probably through relatively small-scale plasmoids, a situation that may also exist at Jupiter.

1. Introduction

[2] The interaction between the solar wind and magnetized planets creates the large scale structures referred to as planetary magnetospheres. Factors that control the properties of a planetary magnetosphere, however, differ at different planets. At Earth, the global configuration and dynamics of the magnetosphere are controlled primarily by the interaction with the external solar wind. In contrast, at Jupiter, although the form of the cavity is still the result of solar wind stresses, many properties of the magnetosphere are determined largely by internal processes associated with the planet's rapid rotation and the stresses arising from internal plasma sources associated with Io and its torus [*Vasyliūnas*, 1983; *Kivelson and Southwood*, 2005]. Saturn, like Jupiter, is a rapidly rotating planet and has significant internal plasma sources (associated with Enceladus and its extended neutral cloud). Both internal and external processes appear to be important in Saturn's magnetosphere (see a review by *Mitchell et al.* [2009a]). At Saturn's orbital distance near 9.6 AU, the low dynamic pressure and weak interplanetary magnetic field of the solar wind might suggest that the role of the solar wind in driving magnetospheric dynamics is secondary to that of internal processes. However, in response to active solar wind conditions such as compressions from Corotating Interaction Regions (CIRs) and from Coronal Mass Ejections (CMEs)

[1]Department of Atmospheric, Oceanic and Space Sciences, University of Michigan, Ann Arbor, Michigan, USA.
[2]Department of Earth and Space Sciences, University of California, Los Angeles, California, USA.

Corresponding author: X. Jia, Department of Atmospheric, Oceanic and Space Sciences, University of Michigan, Ann Arbor, MI 48109-2143, USA. (xzjia@umich.edu)

[*Badman and Cowley*, 2007], the solar wind may affect the dynamics of Saturn's magnetosphere [*Cowley et al.*, 2004].

[3] One manifestation of the solar wind influence on Saturn's magnetosphere is the aurora. Simultaneous observations of the solar wind and Saturn's aurora show that both the size and intensity of the main auroral oval are subject to dramatic changes following the arrival of large solar wind disturbances, such as interplanetary shocks [*Clarke et al.*, 2005; *Crary et al.*, 2005; *Bunce et al.*, 2008]. Among the various solar wind parameters, the dynamic pressure and the convection electric field appear to be the main controlling factors [*Crary et al.*, 2005]. In interpreting the auroral observations obtained during periods of strong solar wind disturbances, *Cowley et al.* [2005] proposed that a strong solar wind compression can induce magnetotail reconnection that closes a significant amount of magnetic fluxes previously opened on the dayside and subsequently transported to the tail, leading to dramatic changes in the global magnetospheric configuration.

[4] The main objective of this paper is to investigate the role of the solar wind in affecting the global configuration and dynamics of Saturn's magnetosphere. To characterize the response of the Kronian magnetosphere to solar wind driving, we have performed a three-dimensional global magnetohydrodynamic (MHD) simulation in which the ionosphere and the magnetosphere are coupled self-consistently. We note that although MHD does not treat kinetic aspects of the plasma system (e.g., particle drift physics), only an MHD model can provide insight into large-scale behavior of the magnetospheric system. Since the focus of this work is the global response of the coupled ionosphere/magnetosphere/solar wind system, an MHD simulation is the appropriate tool for this investigation. Several global MHD simulations of Saturn's magnetosphere [*Hansen et al.*, 2000; *Fukazawa et al.*, 2007a, 2007b; *Kidder et al.*, 2009; *Hansen et al.*, 2005; *Zieger et al.*, 2010] have been carried out previously and they focused mainly on steady solar wind conditions. It has been found during the Cassini mission that structure of the solar wind at Saturn's orbit is dominated by features consistent with those of CIRs, especially during the declining phase of the solar cycle [*Jackman et al.*, 2004]. Correspondingly, in this study we drive our global simulation with a solar wind input that includes features, such as compression and rarefaction, typical of CIRs seen near Saturn and associated with the interaction between the slow and fast solar wind.

[5] The paper is organized as follows. Section 2 introduces the global MHD model and the input parameters. Simulation results are described in section 3 where we first show the global configuration and compare it with observations. We then focus on tail reconnection and its associated dynamics under different solar wind conditions and, finally, we discuss the global convection pattern and the mechanisms through which planetary plasma escapes from the magnetosphere. We conclude with discussion in section 4 and a summary in section 5.

2. MHD Model

[6] The interaction of Saturn's magnetosphere with the solar wind is modeled by using the global, 3D MHD model BATSRUS (Block Adaptive Tree Solar wind Roe-type

Upwind Scheme) together with an Ionosphere Electrodynamics (IE) solver developed by the Center for Space Environment Modeling (CSEM) at the University of Michigan [*Powell et al.*, 1999; *Gombosi et al.*, 2000, 2002, 2004; *Ridley et al.*, 2004]. The BATSRUS model is the Global Magnetosphere (GM) component of the Space Weather Modeling Framework (SWMF) [*Tóth et al.*, 2005] developed to simulate the space environment for various space physics applications [*Tóth et al.*, 2012]. BATSRUS has previously been used by *Hansen et al.* [2000, 2005] and *Zieger et al.* [2010] to model Saturn's magnetosphere. The simulation model presented in this paper is similar to that described in the work by *Hansen et al.* [2005]. In the following, we first introduce the basics of the simulation model and then describe the major differences between the model used in this study and the previous model presented in *Hansen et al.* [2005].

2.1. BATSRUS and Its Adaptation to Saturn

[7] The global MHD model BATSRUS solves the governing MHD equations (conservation of mass, momentum and energy equations together with Faraday's law) with a conservative finite-volume method. A detailed description of the full set of MHD equations and the numerical method can be found in *Powell et al.* [1999] and *Gombosi et al.* [2004].

[8] The BATSRUS model has been adapted to simulate Saturn's magnetosphere by including mass-loading source terms in the MHD equations (for details see *Hansen et al.* [2000]) and further improved by adjusting the spatial distribution of internal plasma sources as well as the mass-loading rates according to recent observations [*Hansen et al.*, 2005]. The main plasma source of water group ions W^+ (H_2O^+, OH^+, O^+, H_3O^+) originating from Enceladus and the rings is included in our global model as an axisymmetric disc-like source centered at 5.35 R_S (R_S = 60268 km, the radius of Saturn) with a scale height of $\sim$0.5 R_S [*Richardson et al.*, 1998], while a secondary plasma source of nitrogen ions N^+ originating from Titan is included as an axisymmetric torus around Titan's orbit at $\sim$20 R_S. Estimates of the total H_2O production rate range from 5.0 $\times$ $10^{27}s^{-1}$ (or $\sim$150 kg/s) [*Fleshman et al.*, 2010] to $\sim$1 $\times$ $10^{28}s^{-1}$ (or $\sim$300 kg/s) [*Jurac and Richardson*, 2005; *Hansen et al.*, 2006; *Burger et al.*, 2007; *Cassidy and Johnson*, 2010]. Recently, *Smith et al.* [2010] reported based on Cassini INMS measurements that the net H_2O production rate at Enceladus varied significantly from pass to pass, ranging from <72 kg/s during the E2 flyby to 750 kg/s during the E5 flyby. Most neutrals escape the Kronian system without being ionized, but some are ionized within the magnetosphere through photoionization and electron impact ionization [*Jurac and Richardson*, 2005; *Bagenal and Delamere*, 2011]. Assuming that $\sim$10% [*Fleshman et al.*, 2010] to 30% [*Jurac and Richardson*, 2005] of the neutrals are ionized, one obtains a net plasma addition rate ranging from $\sim$10 kg/s to 220 kg/s. In the present run, we assume a nominal total mass-loading rate of 3 $\times$ $10^{27}s^{-1}$ for W^+ and 5 $\times$ $10^{25}s^{-1}$ for N^+, corresponding to a total mass-loading rate of plasma of $\sim$85 kg/s assuming an average mass of 16.6 amu for W^+ and 14 amu for N^+, a source rate within the range of estimated rates. In addition to the mass-loading source term, we also include in our MHD model the source term associated with charge-exchange, a process that does
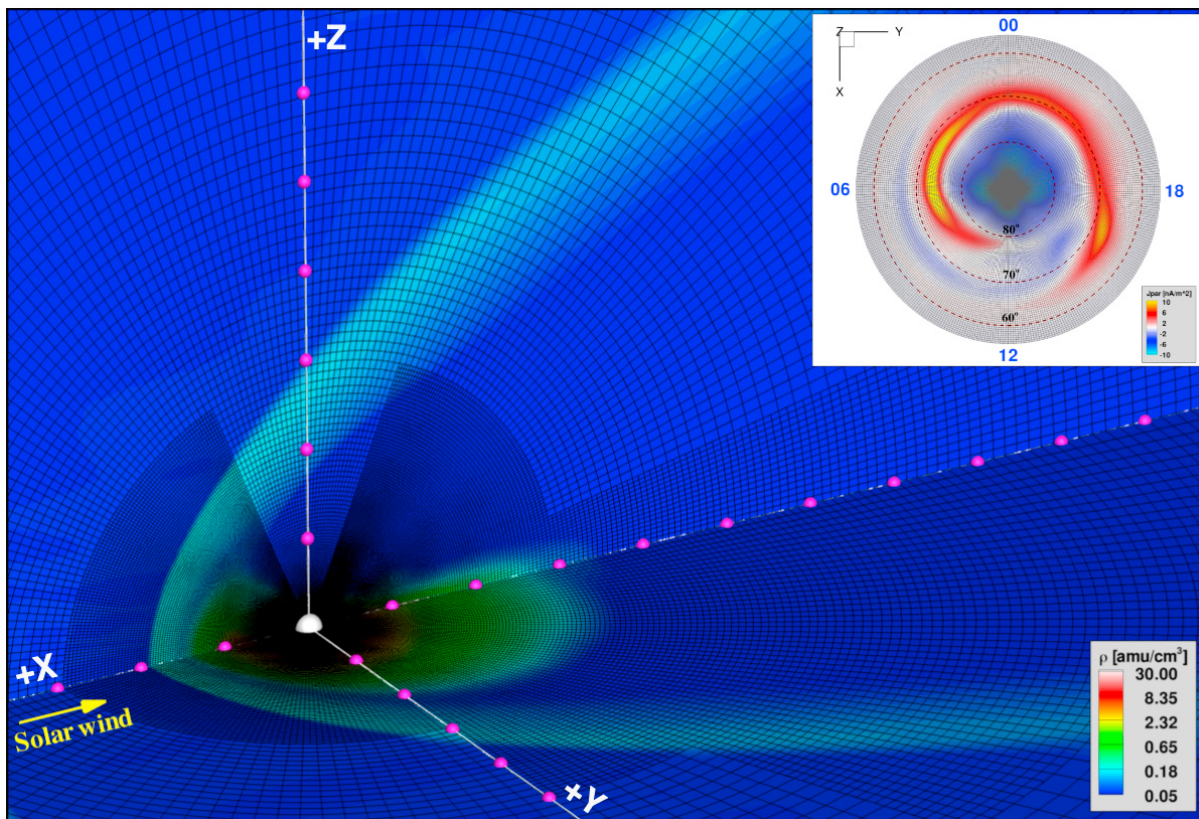
Figure 1. A typical grid distribution in two cuts through a portion of the 3D spherical mesh used in our simulation (viewed from the upstream flank side). These two planes correspond respectively to the XY plane (at Z = 0) and the XZ plane (at Y = 0) in the Kronocentric Solar Magnetospheric (KSM) coordinates with $\hat{X}$ pointing toward the Sun, $\hat{Y}$ being perpendicular to the dipole axis (which is approximately aligned with the rotation axis in the case of Saturn) and pointing toward dusk, and $\hat{Z}$ being chosen so that the dipole axis or rotation axis lies in the XZ plane. Color contours of plasma density are plotted to delineate magnetospheric boundaries, such as the magnetopause and the bow shock. The three Cartesian axes are labeled with magenta balls every 20 R_S. Also plotted is a white sphere of radius 3 R_S, which corresponds to the inner boundary of the global magnetosphere model. Note that high resolution grids are placed in the inner magnetosphere, near the magnetopause and bow shock, and in the magnetotail. The inset shows the grid used in the IE model along with a snapshot of the simulated field-aligned current distribution in the northern ionosphere.

not add mass to the system but affects the momentum and energy exchange of the plasma system by converting hot ions into fast neutrals and replacing them with cold ions. As suggested by *Richardson et al.* [1998], the dominant charge-exchange reaction in Saturn's magnetosphere is the symmetric charge-exchange between O and O^+. The charge-exchange rate in our model is computed based on the results of *Richardson et al.* [1998] that provide information about the oxygen neutral density (peaks at ~4 R_S) and the reaction rate. The total charge-exchange rate used in the present run is ~30 kg/s.

2.2. Simulation Grid

[9] BATSRUS has been implemented with generalized curvilinear coordinates, which provide a smooth mapping from a logically Cartesian grid into a general curvilinear grid, including spherical, cylindrical and toroidal grids [*Tóth et al.*, 2012]. In contrast to previous global MHD models of Saturn's magnetosphere [*Hansen et al.*, 2000; *Fukazawa et al.*, 2007a, 2007b; *Kidder et al.*, 2009; *Hansen et al.*,

2005; *Zieger et al.*, 2010] that all used a Cartesian grid, our new model adopts a high-resolution non-uniform spherical grid. Figure 1 shows a typical grid distribution in two cuts (equatorial and meridional) through a portion of the 3-D spherical mesh used in our model. As shown in Figure 1, owing to the adaptive mesh refinement capability of BATSRUS, the spherical grid used here provides fine resolution in regions of interest: the inner magnetosphere, the magnetospheric boundaries (such as the bow shock and magnetopause) and the equatorial tail current sheet. The grid resolution around the main mass-loading region associated with Enceladus' neutral cloud reaches ~0.1 R_S (between 5 R_S and 10 R_S) and increases to ~0.3 R_S near Titan's orbit (at ~20 R_S). The total number of computational cells reaches ~9 million. Switching from a Cartesian grid such as that used in the previous Saturn simulations by *Hansen et al.* [2005] and *Zieger et al.* [2010] to a spherical grid enables us to better resolve fine structures of the large-scale magnetospheric currents responsible for the coupling between the magnetosphere and ionosphere.

[10] Although we use a spherical grid in order to achieve high resolution in regions of interest, the set of MHD equations is still solved in a Cartesian coordinate system. In order to include as much of Saturn's magnetosphere and the magnetotail as possible at an acceptable computational cost, we set a rectangular computational domain (in which the set of MHD equations is solved) covering the region $-576R_S < X < 96R_S$, $-192R_S < Y, Z < 192R_S$, where X, Y, and Z are the KSM coordinates (refer to Figure 1 for the definition of the KSM coordinates). To avoid the high Alfvén speed close to the planet that greatly limits the allowable time step in the simulation, the inner boundary of the global magnetosphere model is placed at a radial distance of 3 R_S. In the present study, Saturn's rotation and dipole axes are placed along the Z-axis in KSM coordinates and the incident solar wind flow is antiparallel to the X-axis. A centered internal dipole with equatorial surface strength of 20800 nT is used to represent Saturn's internal magnetic field [*Dougherty et al.*, 2005]. For simplicity, we have neglected the higher order moments of the internal field in our simulation but the small differences in internal field models are not significant in the global context.

2.3. Inner Boundary Conditions: Coupling Between BATSRUS and IE

[11] The coupling of the global magnetosphere (modeled by BATSRUS) and the ionosphere (modeled by IE) is handled through field-aligned currents in a relatively simplified way that is used in most Earth magnetosphere models [*Raeder et al.*, 1998; *Lyon et al.*, 2004; *Ridley et al.*, 2004; *Tóth et al.*, 2005; *Hu et al.*, 2007]. Field-aligned currents are calculated at 4 R_S, about 1 R_S beyond the inner boundary of the magnetospheric domain, and then mapped into the ionosphere at ~1 R_S along dipole field lines. Owing to the continuity of electric currents, field-aligned currents must close through horizontal currents in the ionosphere, which is approximated by a resistive and infinitesimally thin layer located at ~1000 km above the 1 mbar level. Closure currents in the ionosphere are then used to derive the distribution of the electric potential and hence the electric field for a given distribution of the ionospheric conductance using a Poisson's solver. The obtained ionospheric electric field is mapped back along dipole field lines from the ionosphere to the magnetosphere under the ideal MHD assumption that magnetic field lines are equipotentials and is then used to calculate the $\vec{E} \times \vec{B}/|B|^2$ drift velocity at the inner boundary, which represents the convection modification resulting from the interaction between the magnetosphere and ionosphere. The rigid corotation flow pattern for a given rotation rate of the planet (Saturn's rotation period is assumed to be 10.5 h in this study as an approximation to the observed periods of Saturn Kilometric Radiation modulation [*Gurnett et al.*, 2009]) is then superimposed onto the calculated convection modification to obtain a modified convection pattern. The modified flow, which is the sum of rigid corotation and the modification resulting from the interaction between the magnetosphere and the ionosphere, then sets the transverse velocity components at the inner boundary of the global MHD model. As an additional inner boundary condition, we set the mass density to 0.1 amu/cm^3 and the temperature to 3 eV at the inner simulation boundary (at 3 R_S).

[12] In addition to the field-aligned currents derived from the global magnetosphere model, the ionospheric conductance is a required input parameter in the IE model. At Saturn, the ionospheric conductance is quite uncertain. Prior estimates of the ionospheric Pedersen conductance, mainly based on Voyager era radio occultations and modeled ionospheric electron density profiles, gave a wide range from 0.1 S to 100 S [*Connerney et al.*, 1983; *Atreya et al.*, 1984; *Cheng and Waite*, 1988]. Recent estimates from calculations using Cassini RSS measurements [*Moore et al.*, 2010] and theoretical studies [*Bunce et al.*, 2003; *Cowley et al.*, 2008] using magnetospheric flow measurements together with auroral observations suggest an ionospheric Pedersen conductance of order several Siemens. In the present study, the northern and southern ionospheres are taken to have uniform Pedersen conductances of 0.5 S and vanishing Hall conductances for simplicity.

[13] To minimize the effects due to interpolation of physical quantities, such as field-aligned currents and convective flow velocity, between those at the inner boundary of the global magnetosphere and those in the ionosphere, it is advantageous to use a fine grid for the IE model whose grid resolution, when mapped along dipole field lines to the inner boundary of BATSRUS, is comparable to the grid resolution of the global magnetosphere model. Therefore, in the IE model, a uniform (θ, φ) mesh (shown in the inset of Figure 1) with 0.5° resolution in latitude (θ) and 1° in longitude (φ) is adopted for the Poisson solver in each hemisphere. The lower (or equatorward) boundary of the IE grid is set at ~55° latitude according to the location of the inner boundary (3 R_S) of the global magnetosphere model.

2.4. Upstream Solar Wind Input

[14] As mentioned earlier, CIRs are structures that are typical of the solar wind at Saturn's orbit and may generate significant impacts on the magnetosphere. To understand the role of solar wind driving in controlling magnetospheric dynamics, we have designed an idealized solar wind input with properties typical of intermittent CIRs seen near Saturn. Figure 2 shows the solar wind and IMF conditions used as input at X = +96 R_S upstream in our model. Throughout the simulation, the IMF magnitude remains fixed at 0.5 nT, but the simulation is divided into four stages each spanning about one week (shaded with different colors in Figure 2). In the successive stages, the field orientation is set southward, dawnward, northward and duskward, respectively. To investigate the interaction of the magnetosphere with interplanetary shocks, an idealized shock structure is introduced in the solar wind within each of the four intervals. In particular, a forward shock is introduced during intervals 1, 3 and 4, whereas a reverse shock is introduced during interval 2 when the IMF is set dawnward. The solar wind flow direction is assumed to be along the Sun-Saturn line (or along the $-\hat{X}$-axis in KSM coordinates). The solar wind plasma temperature is set as 2×10^4 K and the radial component of the IMF (or the IMF B_x in KSM coordinate system) is set to zero in this study.

3. Simulation Results

[15] In this section, we present simulation results with a focus on the global magnetospheric configuration and the
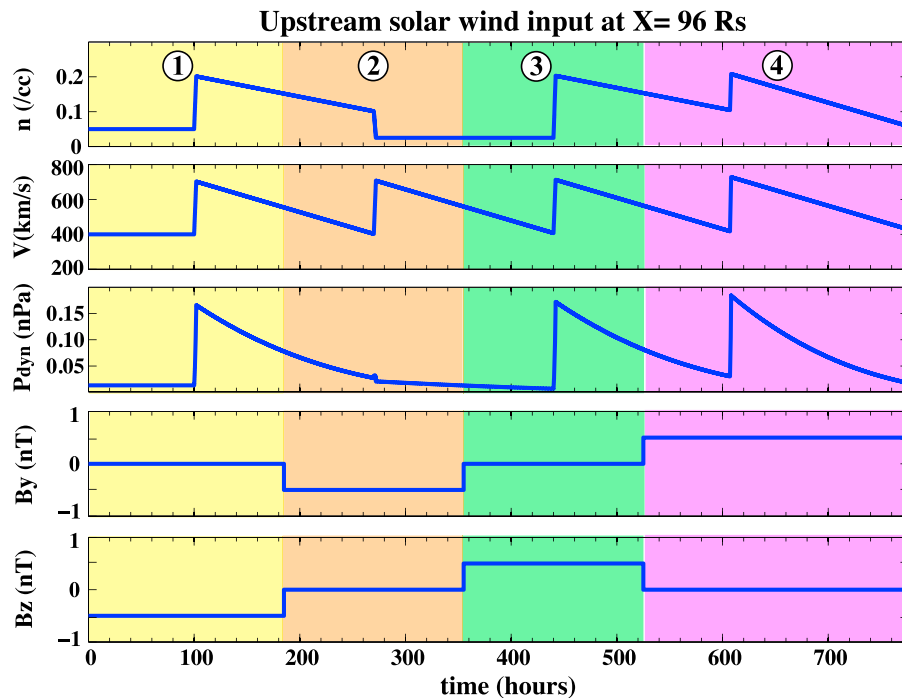
Figure 2. Idealized solar wind input at the simulation outer boundary (at X = +96 R$_S$). The panels from top to bottom show the solar wind number density, speed, dynamic pressure, the IMF B_y and B_z, respectively. The IMF B_x is set to be zero in the simulation. Intervals with different IMF orientations are shaded with different colors.

dynamics associated with reconnection and plasmoid formation in the magnetotail under different solar wind and IMF conditions.

3.1. Global Magnetospheric Configuration: Magnetopause and Bow Shock Locations

3.1.1. Magnetopause Location

[16] The low-latitude magnetopause boundary at equilibrium can be considered approximately as a tangential discontinuity across which the total pressure (the sum of the plasma pressure and magnetic pressure) is balanced. The upstream magnetopause location, therefore, is determined primarily by the balance of the total pressure between the dynamic pressure of the external solar wind and the sum of plasma and field pressures of the magnetosphere. For the Earth's magnetosphere where the internal plasma typically does not contribute much to the total pressure near the magnetopause, magnetic pressure dominates the total pressure on the magnetospheric side of the magnetopause and consequently, the subsolar magnetopause standoff distance (R_{MP}) varies with the solar wind dynamic pressure (P_{dyn}) as a power law $R_{MP} \propto P_{dyn}^{-1/6}$ [e.g., *Spreiter et al.*, 1966; *Sibeck et al.*, 1991; *Shue et al.*, 1997]. In contrast, for Jupiter's magnetosphere where the pressure gradients in the outer magnetosphere are weakened due to the presence of hot plasma and centrifugal stretching in the Jovian magnetodisk, the power law scaling between the subsolar magnetopause standoff distance and the solar wind dynamic pressure has been shown to have a larger exponent between $-1/5$ and $-1/4$ [*Slavin et al.*, 1985; *Huddleston et al.*, 1998]. For the case of Saturn, where the internal plasma source and centrifugal stretching play a considerable (but not as significant

as in Jupiter's case) role in shaping the magnetosphere, the dynamic pressure dependence of the subsolar magnetopause location is believed to be intermediate between those of Earth and Jupiter. Early analysis using Pioneer and Voyager data obtained a terrestrial-type dependence $R_{MP} \propto P_{dyn}^{-1/6}$ [*Slavin et al.*, 1985], while a later study based on Cassini measurements yielded a Jovian-like response $R_{MP} \propto P_{dyn}^{-1/4}$ [*Arridge et al.*, 2006]. More recently, *Kanani et al.* [2010] improved the analysis of *Arridge et al.* [2006] by including the suprathermal plasma contributions and also considering variable static pressures in the pressure balance equation. The new analysis of *Kanani et al.* [2010] gave a power law index of ~1/5 for the dependence of the subsolar magnetopause location on the solar wind dynamic pressure, indicating that Saturn's magnetopause is neither as rigid as the Earth's nor as compressible as Jupiter's [*Achilleos et al.*, 2008].

[17] Our simulation provides a new way of investigating the standoff distance of Saturn's magnetopause. As introduced in section 2.4, the solar wind input used in our model is designed to mimic typical CIR-dominant solar wind structures at Saturn and consequently, the upstream solar wind pressure is not constant throughout the whole simulation but time-varying. Such a solar wind input, therefore, enables us to examine how the global magnetospheric configuration changes in response to the external conditions and to compare the simulated behavior of the magnetosphere with that inferred from in-situ observations. In particular, here we compare the magnetopause standoff distances extracted from the MHD simulation at multiple time steps with the predictions from the empirical magnetopause model developed by *Kanani et al.* [2010] (hereinafter referred to as
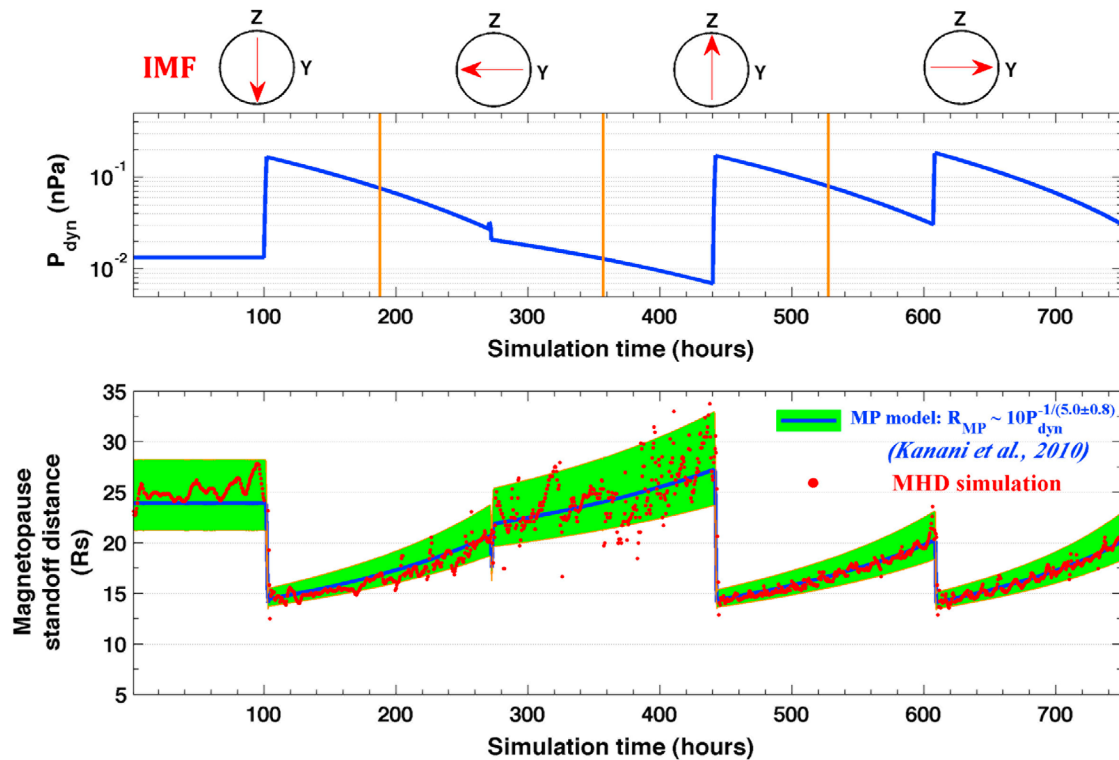
Figure 3. Comparison of the magnetopause standoff distance between the MHD simulation and the magnetopause model of *Kanani et al.* [2010] constructed based on Cassini observations. (top) The upstream solar wind conditions, including the IMF orientation (indicated by the red arrows) and the dynamic pressure. The vertical orange lines mark the times when the discontinuities of IMF rotation arrive at the nose of the magnetopause. (bottom) The red dots show the standoff distance extracted from the MHD simulation and the blue trace along with the green shaded area indicate the standoff distance predicted by the magnetopause model of *Kanani et al.* [2010] ($R_{MP} \propto P_{dyn}^{-1/(5.0\pm0.8)}$).

"K10") implied by previous discussion. Figure 3 shows the comparison along with the instantaneous upstream solar wind dynamic pressures and IMF orientations. The prediction from the K10 model is calculated based on the functional form $R_{MP} \sim 10P_{dyn}^{-1/(5.0\pm0.8)}$ by using the solar wind dynamic pressures in our simulation input, and the predicted mean locations and variations are represented by the blue trace and the green-shaded area, respectively, in the bottom panel of Figure 3. The magnetopause standoff distances extracted from the MHD simulation are shown as red dots in Figure 3.

[18] Several points regarding the comparison are worth mentioning here. Throughout the whole simulation, the magnetopause standoff distances in our MHD model agree well with that predicted by the K10 magnetopause model. In particular, both the mean values and variations of the subsolar locations in our MHD model are consistent with those predicted by the K10 model for various dynamic pressure values in the range considered. As can be seen from the K10 model, the lower the solar wind dynamic pressure, the larger the variation in the size of the magnetosphere. The modeled magnetosphere shows similar behavior. For instance, between T = 280 and T = 440 h when the dynamic pressure is low, the magnetopause boundary of the simulated magnetosphere experiences large displacements.

[19] In a previous modeling study, *Hansen et al.* [2005] also compared the simulated boundary crossings from their

MHD simulation with Cassini measurements during SOI and obtained a good agreement. The solar wind dynamic pressures considered in the study of *Hansen et al.* [2005] range from 0.007 to 0.03 nPa. For comparison, the upstream solar wind dynamic pressure used here covers a broader range from 0.005 to 0.2 nPa. This range is consistent with that inferred from the propagated solar wind conditions at Saturn using measurements at 1 AU [*Zieger and Hansen*, 2008]. Therefore, the solar wind conditions used in the present simulation extends the data set for testing the dependence of the magnetopause standoff distance on the solar wind dynamic pressure.

[20] As the magnetopause is a boundary that is principally determined by the pressure balance between the pressures outside and inside of the magnetosphere, the location of the magnetopause presumably does not depend significantly on the IMF orientation. The K10 magnetopause model does not include any dependence on the IMF orientation. However, under certain IMF conditions, such as during periods of northward IMF, magnetopause reconnection may erode the dayside magnetosphere and consequently may cause the magnetopause to move closer to the planet. It is therefore interesting to examine in our model how the dayside magnetopause location depends on the IMF orientation. Comparing the simulated magnetopause locations at times when the solar wind dynamic pressure is the same but the IMF orientation is different shows that the subsolar magnetopause
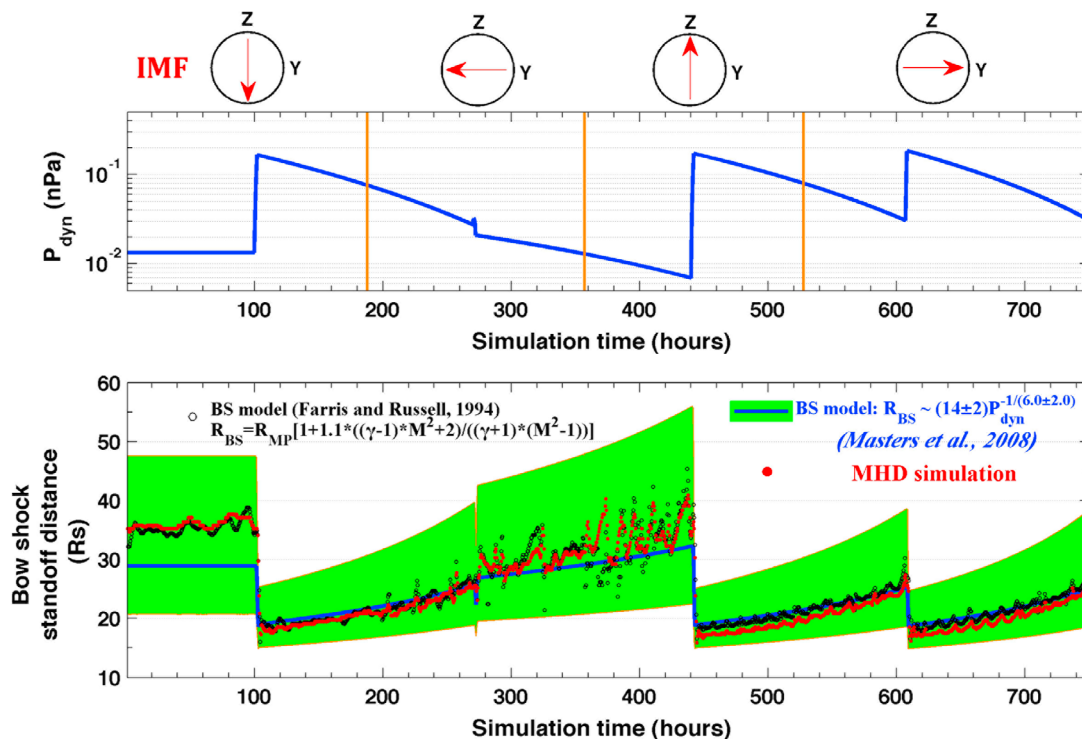
Figure 4. Comparison of the bow shock standoff distance between the MHD simulation and two empirical models of the bow shock. As in Figure 3, (top) the upstream solar wind conditions, including the IMF orientation (indicated by the red arrows) and the dynamic pressure; (bottom) the red dots show the standoff distances extracted from the MHD simulation and the blue trace along with the green shaded area indicate the standoff distances predicted by the bow shock model of *Masters et al.* [2008] ($R_{BS} \sim (14 \pm 2)P_{dyn}^{-1/(6.0\pm2.0)}$) constructed using Cassini observations. The black circles represent the standoff distances predicted by the model of *Farris and Russell* [1994] originally developed for the Earth's bow shock. The standoff distance in this model is given as $R_{BS} = R_{MP}\left[1 + 1.1\frac{(\gamma-1)M^2+2}{(\gamma+1)(M^2-1)}\right]$, which depends on the upstream solar wind magnetosonic Mach number M, the magnetopause standoff distance R_{MP} and the ratio of specific heats γ taken as 5/3.

distances are roughly the same. Our model results, therefore, suggest that the location of Saturn's magnetopause is quite insensitive to the IMF orientation.

3.1.2. Bow Shock Location

[21] Another important magnetospheric boundary is the bow shock. We next compare bow shock locations in our MHD model with the locations predicted by empirical models constructed based on in-situ observations. Several empirical models have been developed to describe the location and the overall shape of Saturn's bow shock [*Slavin et al.*, 1985; *Hendricks et al.*, 2005; *Masters et al.*, 2008; *Went et al.*, 2011]. The empirical model of *Masters et al.* [2008] (hereinafter referred to as "M08") was constructed using bow shock observations from Cassini as well as the Pioneer and Voyager spacecraft. Figure 4 compares the simulated subsolar bow shock distances (red dots) with the predicted values from the M08 model (the blue trace shows the mean distance and the green area shows the range). The comparison shows that the simulated shock distances are in good agreement with the mean predictions from the M08 model for most of the simulation interval. However, there are significant differences between the modeled location and the mean location from the M08 model during some intervals, i.e., the interval prior to T = 100 h and the interval between

T = 280 and T = 340 h, although the MHD model results fall within the predicted range given by the M08 model, which, in general, is quite large due to the approximations made in the model construction (e.g., the assumption of constant upstream solar wind speed). Both intervals correspond to relatively low solar wind dynamic pressure conditions, $P_{sw}< \sim 0.02$ nPa. It should be noted here that most of the data used to construct the M08 model correspond to dynamic pressure values above 0.02 nPa and only very few data points are below 0.02 nPa [see *Masters et al.*, 2008, Figure 6]. Therefore, it is likely that the lack of sufficient observations under low dynamic pressure conditions leads to inaccurate predictions of the M08 model in this range.

[22] As the bow shock is a structure formed when supersonic solar wind flow encounters the magnetosphere, the incident flow conditions (e.g., flow Mach number) and the shape and size of the magnetosphere are the primary factors in determining the location and shape of the bow shock. In the terrestrial case, a number of models have been developed to describe the properties of the bow shock based on the properties of the upstream solar wind and the magnetopause. Among these, the model of *Farris and Russell* [1994] has extended previous empirical models by taking into account the behavior of the shock under low Mach number conditions.
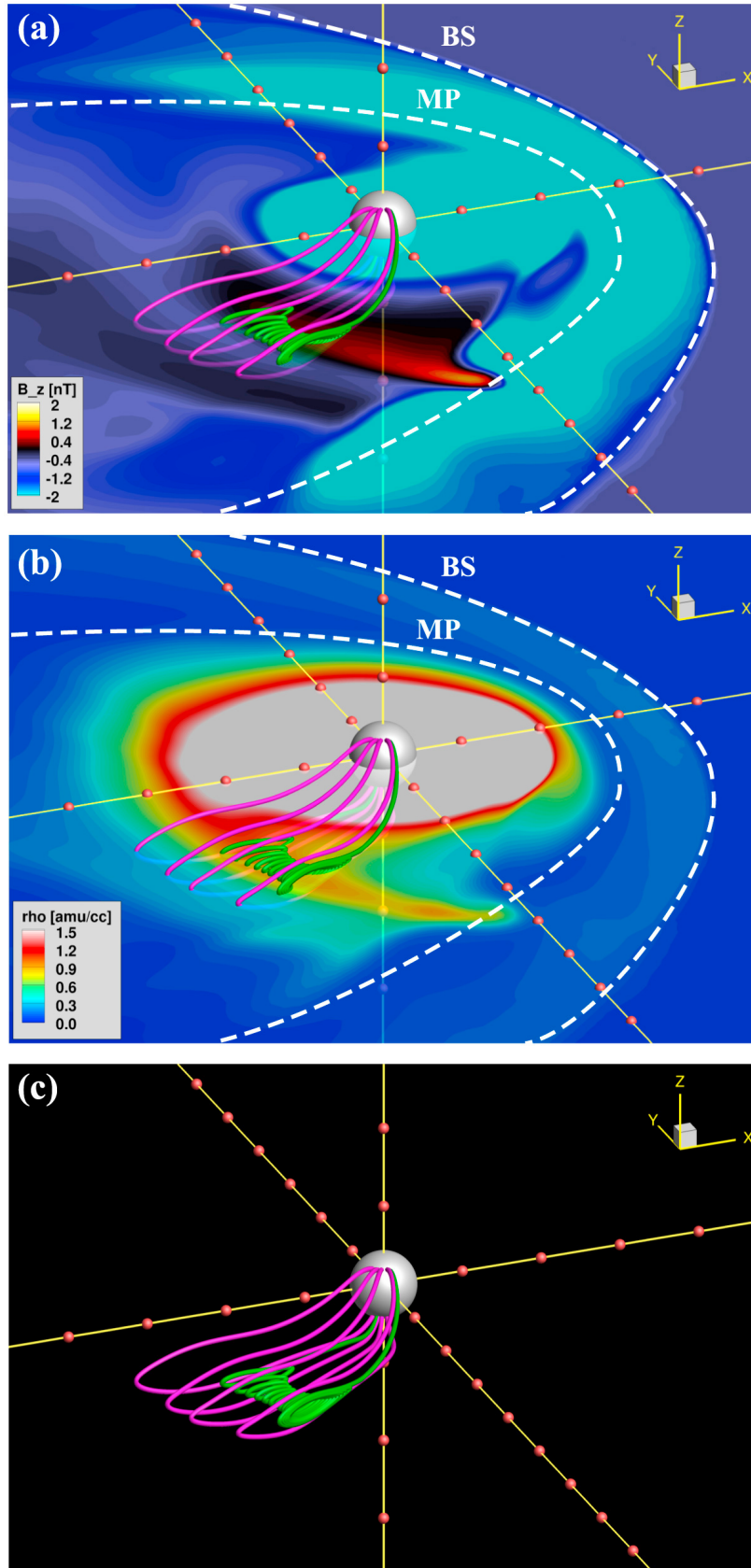
Figure 5

In the *Farris and Russell* [1994] model the bow shock subsolar standoff distance (R_{BS}) is linked to the magnetopause standoff distance (R_{MP}) and the solar wind magnetosonic Mach number (M_{ms}) as shown by the formula: $R_{BS} = R_{MP}\left[1 + 1.1\frac{(\gamma-1)M_{ms}^2+2}{(\gamma+1)(M_{ms}^2-1)}\right]$, where $\gamma = 5/3$ is the ratio of specific heats. While the lack of simultaneous measurements of upstream solar wind and boundary crossings greatly limits the development of an empirical model of a similar kind at Saturn, our MHD simulation provides a useful means to test whether or not such a terrestrial model can be applied to the case of Saturn. In Figure 4, the black circles show the predicted subsolar standoff distances of the *Farris and Russell* [1994] model computed by using the simulated magnetopause standoff distances shown in Figure 3 together with the magnetosonic Mach number of the upstream solar wind (obtained directly from the input parameters of our model). It is clear from the figure that the *Farris and Russell* [1994] model predictions closely match the MHD model results throughout the whole simulation interval including the aforementioned intervals of unusually low solar wind dynamic pressure. The good agreement thus suggests that this terrestrial bow shock model can provide a good description of the bow shock location at Saturn.

[23] In summary, we find based on the comparisons presented above that the M08 bow shock model provides a reasonably good estimate of the shock standoff distance under medium and high solar wind dynamic pressure conditions. Our model results, however, indicate that under low dynamic pressure conditions, the M08 model underestimates the shock standoff distance and a better description of the shock location that takes into account the upstream solar wind Mach number and the size of the magnetopause, such as the bow shock model of *Farris and Russell* [1994], should be employed.

3.2. Reconnection in the Magnetotail and Its Effects on the Magnetosphere

[24] A key process involved in magnetospheric dynamics is reconnection in the magnetotail. In this section we focus on large-scale reconnection and associated plasmoid formation in the magnetotail and other aspects of magnetospheric dynamics under different upstream conditions.

3.2.1. Tail Reconnection and Plasmoid Formation for Southward IMF

[25] As first proposed by *Vasyliūnas* [1983] in a Jovian context, in a rotationally driven magnetospheric system, reconnection occurs on mass-loaded closed field lines, which are stretched due to centrifugal acceleration, form an X-line and eventually pinch off producing tailward-moving plasmoids. The release of plasmoids down the tail carries away the plasma previously added to the closed flux tubes in the inner magnetosphere. Such a process provides a means for removing plasma from the magnetosphere while conserving the total flux of the planetary internal field. To see if such an internally driven process is operating at Saturn, we first analyze interval 1 of the simulation when the IMF is southward (see Figure 2), parallel to planet's internal field near the equator. Under such circumstances, effects of the solar wind, such as dayside reconnection, are expected to be minimal and the whole magnetosphere is essentially closed. Such a state of the magnetosphere allows us to focus on processes that are predominantly internally driven.

[26] Figure 5 shows an example of a plasmoid formed during simulation interval 1 (at T = 90 h). It should be noted here that the plasmoid formation evolves with time in the model and Figure 5 represents only a snapshot of the early stage of the plasmoid development. The plasmoid is identified from magnetic field signatures. In Figure 5a the background colors represent contours of the north-south component of the magnetic field (B_z in the KSM coordinates) in the equatorial plane. We note that the modeled current sheet lies in the equatorial plane and B_z in the equatorial plane is equivalent to B_θ in the spherical coordinate system KRTP that has been commonly used in Cassini data analysis of plasmoid events [e.g., *Jackman et al.*, 2007]. In this plane, B_z is generally negative inside the magnetosphere, i.e., it has the same polarity as the planetary field. However, when a plasmoid forms in the current sheet, its magnetic topology implies both negative and positive polarities of field components, resulting in bi-polar variations in the normal component of the magnetic field. The normal component, B_z, vanishes both in the center of the plasmoid and at the X-line where the plasmoid pinches off. Such magnetic signatures are commonly used as proxies for identifying plasmoids. As shown in Figure 5a, a region of positive B_z (anti-parallel to the planetary field) encompassed by boundaries of zero B_z (black color) is present in the quadrant between midnight and dawn, indicative of reconnection and plasmoid formation. This is confirmed by the configuration of magnetic field lines traced through that region. The green traces in Figure 5a show the magnetic topology of the plasmoid identified, which is composed of loop-like field lines with very weak core fields (in the direction normal to the cross-section of the plasmoid). The total magnetic field strength (not shown in the figure) shows a minimum near the center of the plasmoid. At this particular stage of the plasmoid formation, the plasmoid is still connected to the planet at their ends because of the finite extent of the reconnection region but it is eventually released when reconnection occurs at the ends of the structure. Figure 5b shows the same view as Figure 5a but with color contours of plasma density in the equatorial plane. It can be seen that the plasma density inside the plasmoid is higher than in the surroundings. Because the whole magnetosphere in this case is closed, all of the field lines are closed. The plasmoid, even after pinching off at the X-line, is surrounded by closed field lines with both ends connected to the planet (shown as magenta traces). These closed field lines tailward of the plasmoid appear to confine the plasmoid and to prevent it from moving directly downtail. On the other hand, the

Figure 5. 3D perspective (as viewed from the north near the dawnside flank) of the structure of a plasmoid formed under southward IMF condition (at T = 90 h). Color traces are sampled field lines extracted from the simulation with green showing field lines that thread the plasmoid and magenta showing field lines that surround the plasmoid. (a, b) The background colors represent contours of B_z and plasma mass density in the equatorial plane, respectively. The two dashed lines show the bow shock and magnetopause boundaries identified by tracing flow streamlines. (c) Selected magnetic field lines within and in the immediate vicinity of the plasmoid. In each plot, orange balls mark every 10 R_S along the axes.

plasma within the plasmoid still carries angular momentum resulting from magnetospheric convection. Thus it continues to move primarily in the $-\hat{Y}$ direction toward the magnetopause on the dawn flanks. As a result, the tail X-line associated with plasmoid formation extends from the near-midnight region to the dawnside magnetopause, as indicated by the positive B_z contours and the structure of enhanced density in Figures 5a and 5b. As the plasmoid reaches the magnetopause, it interacts with the magnetosheath plasma through reconnection and eventually escapes from the magnetosphere and merges with the sheath flow.

[27] Given that the modeled magnetosphere during interval 1 is basically closed and the solar wind influences are minimal, it is clear that the plasmoid shown above is a product that results from internal process, i.e., the so-called Vasyliūnas-cycle in which the planet's rapid rotation combined with the mass-loading of flux tubes associated with the internal plasma sources (Enceladus and its neutral cloud) lead to reconnection on closed field lines. The plasma content of the plasmoid is lost from the magnetosphere by the subsequent plasmoid release on the dawn flank.

3.2.2. Tail Reconnection and Plasmoid Formation for Spiral IMF

[28] The preceding section discusses reconnection and plasmoid formation for a strictly southward IMF condition. Although such an IMF condition may be rare at Saturn, the model results provide insights into how internal processes affect the configuration and dynamics of the magnetosphere. Next we focus on tail reconnection and related magnetospheric dynamics for a more typical IMF condition at Saturn, i.e., for a Parker spiral IMF orientation with B_y dominant [*Jackman et al.*, 2008]. When the IMF switches from a southward to a spiral orientation, dayside reconnection between the IMF and the planetary field is expected to occur on the dayside magnetopause. Dayside reconnection implies that the polar cap and thus the tail lobes are populated with open field lines, in contrast to the situation during interval 1 when the IMF is purely southward.

[29] During interval 2 of the simulation, with the IMF orientation close to the spiral angle, several large-scale tail reconnection events are seen. We take one of the reconnection events (around T = 224 h) as an example of the characteristics of reconnection and the resultant dynamics. Figure 6 shows the contours of B_z (colors) and the plasma density (lines) in the equatorial plane extracted from the time step T = 225 h (about an hour after the reconnection occurs). According to the criteria for identifying reconnection events discussed above, the region of strong positive B_z in the tail indicates tail reconnection. Field lines traced near the region of the B_z reversal show flux rope-like geometry. At this instant, part of the plasmoid structure is still attached to the planet. As the simulation evolves, the plasmoid eventually detaches from the magnetosphere through reconnection with the surrounding medium. As in the case of southward IMF, the plasma density within the plasmoid is higher than in the surroundings as evident from the line contours. Planetward of the plasmoid there exist some field lines (low plasma density, hence blue) with both ends in the solar wind. As mentioned above, for a spiral IMF orientation, dayside magnetopause reconnection produces open field lines that are then transported to the magnetotail. The transport timescale

for open field lines from the dayside magnetopause to the tail is of order tens of hours depending on the upstream solar wind and IMF conditions. The field lines planetward of the plasmoid are newly reconnected field lines arising from reconnection between the open field lines previously stored in the tail lobes. The low plasma densities on those field lines are consistent with being products of reconnection between lobe field lines. Moreover, the $B_z = 0$ contour line (black color in Figure 6) planetward of the solar wind field lines (blue lines) indicates the location of the tail X-line, which is at $X \sim -30$ R_S near midnight. For this plasmoid event, the X-line initially is located at $X \sim -25$ R_S near midnight. As the simulation evolves, the plasmoid moves downtail and the X-line retreats in the tailward direction. By the time when the plasmoid reaches $X = -80$ R_S, the X-line moves to $X \sim -30$ R_S near midnight. We note that in general, the X-line location in our model varies with time as a result of both the time-varying upstream solar wind conditions and temporal evolution of the system. The radial range of the X-line location identified in our model is from ~ 25 R_S to ~ 40 R_S, consistent with the radial distance (30 to 40 R_S) suggested by *Jackman et al.* [2011] regarding where plasmoids may typically form in Saturn's magnetotail.

[30] In the simulation, we have placed a series of virtual spacecraft (v/s) at various locations in the magnetosphere to identify the variations in field and plasma parameters associated with magnetospheric dynamics that would be observed by spacecraft instruments. In Figure 7a, we show the modeled magnetic field and plasma conditions seen by a v/s located at $X = -80$ R_S, $Y = 0$ downtail in the equatorial plane. We note that among all the virtual spacecraft placed in this run, the one presented here is the one that is tailward of the reconnection site and closest to where Cassini was. Results are shown only for the several hour interval around the time when the plasmoid shown in Figure 6 passes the v/s. Here the model results are presented in a spin-aligned spherical coordinate system (r, θ, ϕ) to enable direct comparison with Cassini data. During the passage of the plasmoid, the v/s sees a bi-polar variation in the B_θ component and an enhancement in the core field (B_ϕ) at the center of the plasmoid, identified as the time of B_θ reversal. Plasma density and pressure are enhanced within the plasmoid and peak at the center of the plasmoid. An interesting feature in the B_θ variation is worth noting here. In addition to the bi-polar signature expected for a plasmoid, the B_θ component remains negative (northward) for an extended interval before it returns to its initial state (small positive values). Also seen during this interval is rapid plasma outflow primarily in the radial direction with speeds of order 1000 km/s (bottom panel in Figure 7a), accelerating the plasmoid downtail. The structure characterized by the prolonged recovery of B_θ and fast plasma flows that appears behind the plasmoid corresponds to the region containing reconnected field lines produced by lobe-lobe reconnection shown in Figure 6. The high flow speed (~ 1000 km/s) is consistent with that expected for the speed of outflows (which is of order of the inflow Alfvén speed) generated by reconnection between lobe field lines, where the Alfvén speed is high due to the low plasma density. The total field strength seen during this modeled event shows an enhancement near the center of the plasmoid and reaches maximum in the post-plasmoid region due to the compression by the fast outflows behind the plasmoid.
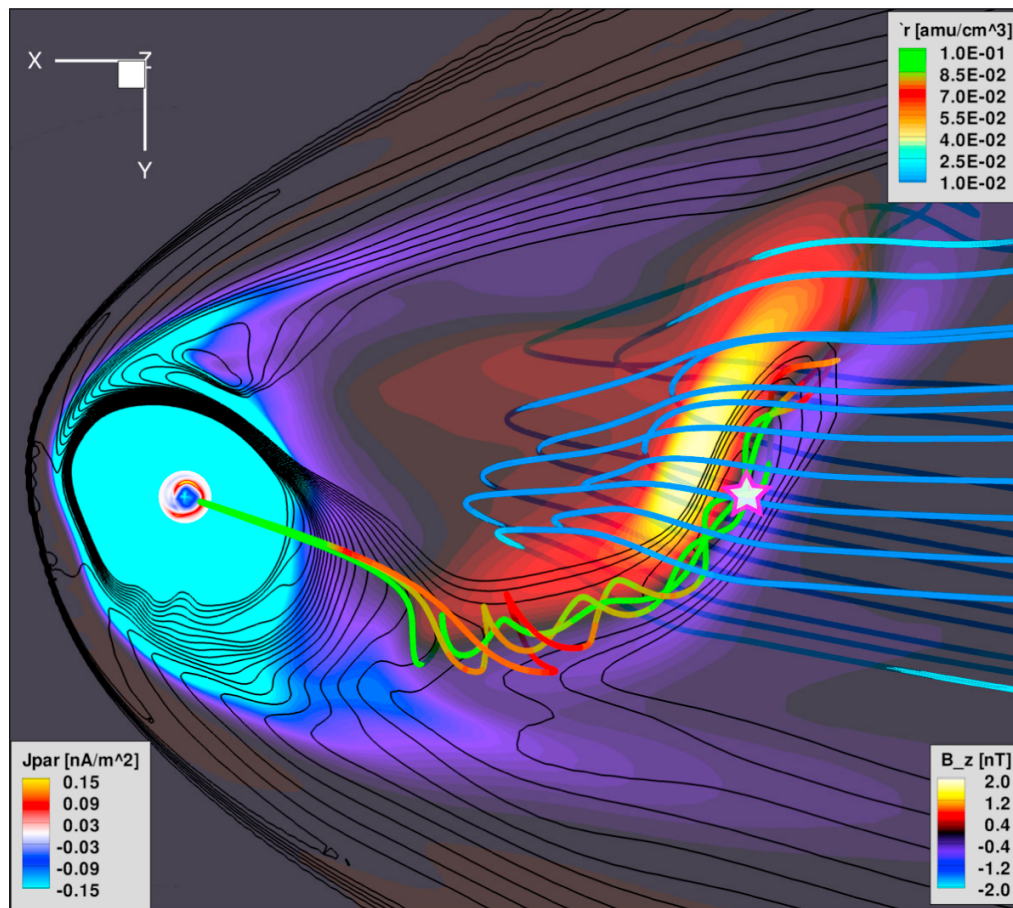
Figure 6. 3D structure of a plasmoid formed in the simulation (at T = 225 h) with the IMF roughly aligned with the spiral angle. Shown in the background are color contours of B_z (according to the bottom-right color bar) and line contours of plasma density in the equatorial plane. Selected field lines showing the magnetic structure of the plasmoid are color coded with plasma density (according to the top-right color bar). The pattern of field-aligned currents in the ionosphere is also shown (mapped to a sphere of radius 4 R_S for clarity). The magenta star in the tail marks the position of a virtual spacecraft placed in the simulation for observing plasmoids (results are shown in Figures 7 and 9).

[31] Plasmoids in Saturn's magnetotail have been observed by Cassini and for a few published cases both plasma and field measurements were acquired. It is interesting to compare the characteristics of the plasmoid identified in our model with in-situ measurements. Figure 7b shows Cassini field and particle observations during a plasmoid event that occurred on March 4th, 2006 [*Jackman et al.*, 2007; *Hill et al.*, 2008], one of few plasmoid events with plasma moments data available [*Hill et al.*, 2008]. One should not anticipate detailed representation of the data on individual Cassini orbits for several reasons. For example, the upstream solar wind and IMF conditions used in our simulation are highly idealized and may not represent the external conditions during which Cassini measurements were acquired. Moreover, the sampled virtual spacecraft is located further downtail compared to the Cassini spacecraft, so the duration of the modeled plasmoid event is longer than the Cassini event because the plasmoid expands (the cross-section area increases) as it moves downtail. Nonetheless, we find that the plasmoid structure in our simulation has many features similar to those seen in in-situ measurements. As shown in

Figure 7b, the observed magnetic field during this event shows an enhancement of the core field (B_ϕ) near the center of the event and a bi-polar variation in the B_θ component. Moreover, plasma density increases near the center of the plasmoid. All of these features are similar to what is seen in our model results described above. The measured flow velocity also shows strong outflows with maximum speed of 800 km/s right behind the plasmoid itself, during an interval in which B_θ remains at small negative values. Such high outflow speed corresponds well to the flow speed seen in the modeled plasmoid event.

[32] We note that the field and plasma characteristics in the region behind the plasmoid as seen both in our model and in the Cassini event are quite similar to those seen in the so-called "Post-Plasmoid Plasma Sheet" (PPPS) in Earth's magnetotail [*Richardson et al.*, 1987], which appears to play an important role in magnetic flux transport down tail. Recently *Jackman et al.* [2011] did a survey on Cassini magnetometer data focusing on the magnetic signatures associated with plasmoids. Their analysis showed that plasmoids events at Saturn often are followed by an extended
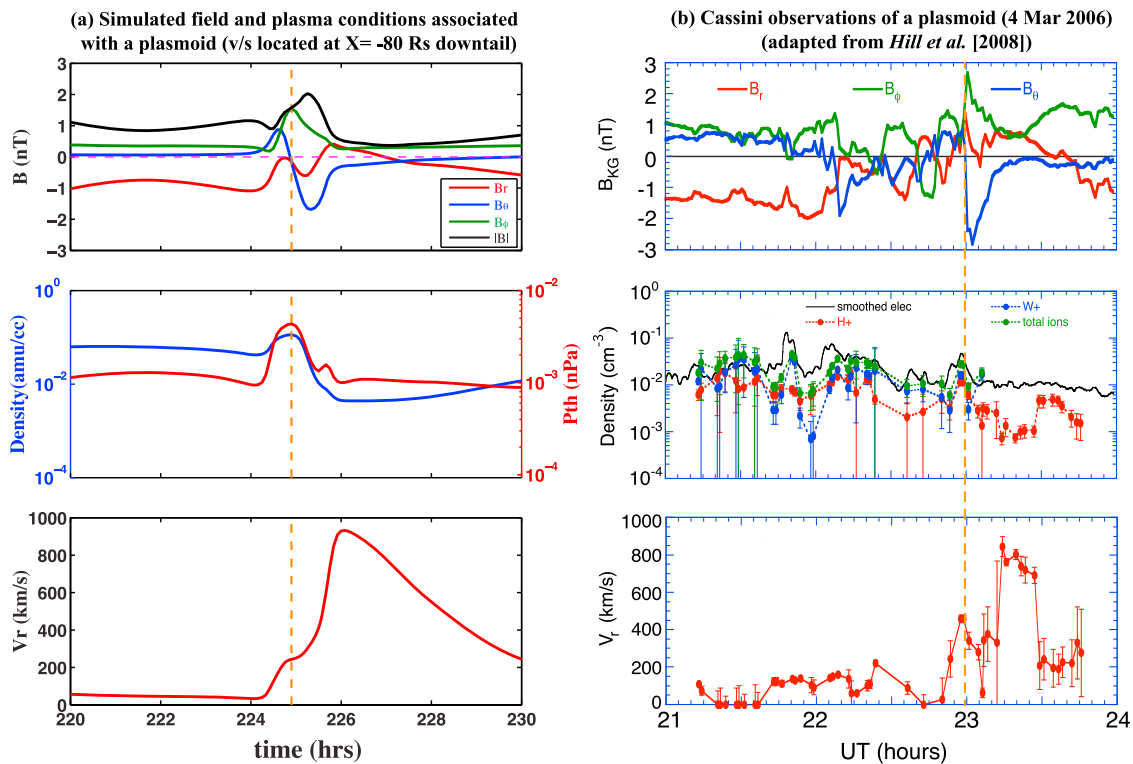
Figure 7. Comparison of modeled plasmoid signatures with those seen in Cassini in-situ observations of plasmoid. (a) Modeled plasmoid signatures seen by a virtual spacecraft (v/s) located at $(X, Y, Z) = (-80, 0, 0)$ R_S downtail. Shown from top to bottom are magnetic field components in spherical coordinates and field magnitude, plasma density (in blue) and thermal pressure (in red), and radial velocity, respectively. (b) Cassini MAG and CAPS data for the plasmoid event on 6 March 2006 shown in *Hill et al.* [2008]. During this event, Cassini was located near 0300 local time at a distance of 44 R_S near the equator. The dashed vertical lines in both plots mark the central event times identified based on the characteristics of B_θ.

interval of the PPPS. They also estimated the amount of magnetic flux closed during each plasmoid and tail reconnection event based on the magnetic field observations of PPPS. We will compare our model results with their statistical analysis in section 3.3.

[33] Reconnection in the tail not only produces plasmoids traveling down tail as discussed above but also generates significant impacts on the magnetosphere on the planetward side. Figure 8 shows the dynamical response of the magnetosphere planetward of the reconnection site for the reconnection event (at T = 225 h) shown in Figure 6. As shown by the background colors, which represent contours of the ratio between the azimuthal flow velocity and rigid corotation speed, plasma flows in most of the magnetosphere are subcorotational. However, there is a channel of rapidly moving flows in the midnight-to-dawn sector. Associated with those fast flows are relatively low plasma densities (as indicated by the line contours) and high temperatures (not shown in the figure). Those hot and rapidly moving flux tubes are return flux tubes produced by the tail reconnection [*Masters et al.*, 2011]. As shown by the green traces in Figure 8, those flux tubes are closed with both ends attached to the planet. They carry magnetic flux closed through tail reconnection and return it to the dayside. In a theoretical model proposed by *Cowley et al.* [2005], the authors discussed the role of Dungey-cycle in affecting global plasma and magnetic flux

circulation in Saturn's magnetosphere and predicted that an X-line forms in the post-midnight sector due to the reconnection between open field lines in the tail. We find that the reconnection configuration and the resulting circulation pattern in our simulation are generally consistent with the picture proposed by *Cowley et al.* [2005].

[34] Flow shears and/or pressure gradients in the magnetosphere often produce field-aligned currents (FACs) that flow into the ionosphere. In the example presented here, those rapidly moving return flux tubes indeed generate strong disturbances in the ionosphere. As shown by the sampled field lines in Figure 8 the region of fast flows in the magnetosphere maps to a region in the ionosphere with intense upward FACs, which can be seen more clearly in the insert in top-right corner of Figure 8. The FACs intensification appears to be strongest near dawn as the flux tubes move from the nightside to the dayside. We note that the ionospheric signatures are more intense in this case than in the reconnection event discussed in section 3.2.1 that does not involve lobe reconnection. Where upward current becomes sufficiently intense, field-aligned electric fields commonly develop to accelerate the current-carrying electrons. Accelerated electrons, in turn, may generate auroral emissions. Our simulation results, therefore, suggest that the intensification of FACs associated with tail reconnection involving open flux may produce auroral brightenings in the dawnside
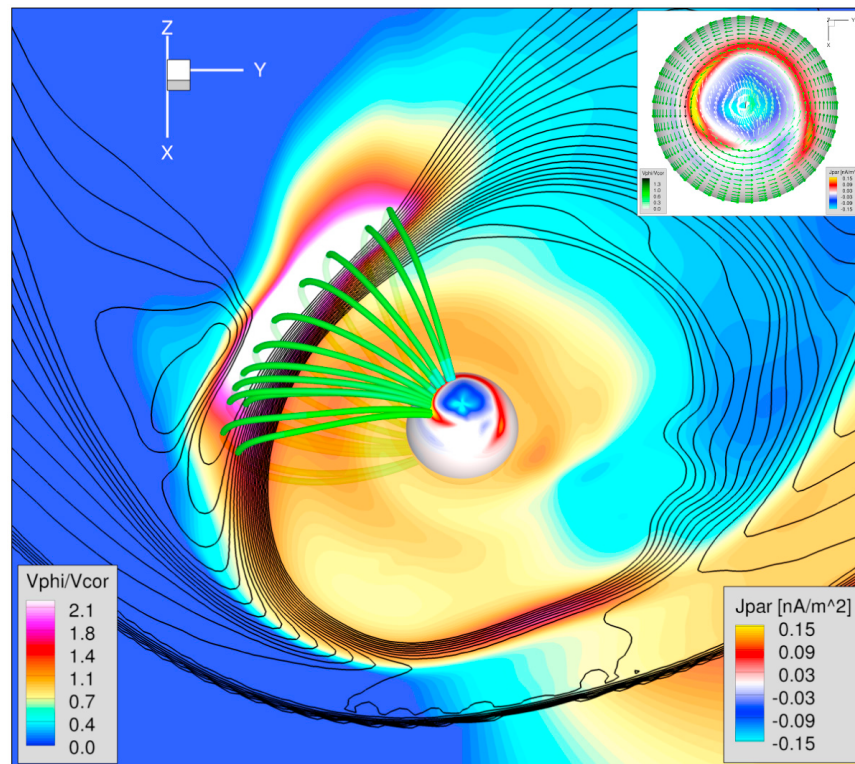
Figure 8. A 3D perspective from a viewpoint above the equator in the noon meridian plane of the flux tubes returning from tail reconnection site to the magnetosphere as seen in the simulation at T = 225 h. Plotted in the equatorial plane are color contours of Vphi/Vcor overlaid with line contours of plasma density. The pattern of field-aligned currents along with unit flow vectors color coded with Vphi/Vcor in the northern ionosphere are shown in the inset as well as in the magnetospheric plot (mapped to a sphere of radius 4 R_S for clarity). Green traces show some sampled field lines traced through the region of rapidly moving flows in the magnetosphere.

ionosphere such as those seen in the aurora observed at Saturn [*Clarke et al.*, 2005; *Mitchell et al.*, 2009b].

3.2.3. Effects of the External Solar Wind on Tail Reconnection and Plasmoid Formation

[35] In sections 3.2.1 and 3.2.2 we presented two typical examples of tail reconnection from our simulation. There are many large-scale reconnection and plasmoid events with features similar to those seen in the two representative cases during the ~700 h simulated. Because the external conditions change during the run, it is possible to examine how the properties of tail reconnection, such as the repetition time, vary with the changing solar wind conditions. Here we use the modeled field and plasma conditions observed by a virtual spacecraft in the tail as a way of illustrating the behavior of the system.

[36] Figure 9 shows the model results for the same v/s (at X = −80 R_S) shown in Figure 7a but for the whole simulation interval. The times when the v/s encounters large-scale reconnection and plasmoid events can be readily identified by the flow bursts and changes in the magnetic field, especially the bi-polar variations in the B_θ component. Large scale reconnection events are seen repeatedly by the v/s during most of the simulation interval except in interval 1 mainly because the v/s is at a fixed location in the midnight meridian while most of the plasmoid events that occur during interval 1 are seen in the post-midnight sector. Based on

results shown in Figure 9, we find that the repetition time of tail reconnection varies with the upstream solar wind conditions. In particular, the repetition time ranges from 20 to 40 h when the solar wind dynamic pressure is relatively low and the size of the magnetosphere is relatively large to a time close to the planetary rotation period when the magnetosphere is compressed by a forward shock, as occurred during intervals 3 and 4 (grey shaded intervals). Such periodic behavior, however, only lasts for several cycles and thereafter the repetition time of plasmoid formation increases as the solar wind pressure gradually decreases. Given that the total mass input rate associated with Enceladus and its neutral cloud is fixed throughout the simulation, our model results suggest that the external solar wind plays an important role in affecting the periodicity of dynamics in Saturn's magnetosphere.

3.3. Open Flux Variations in the Magnetosphere

[37] A parameter useful for characterizing the global response of the system to changes in the solar wind-magnetosphere coupling and changes in the global configuration associated with magnetospheric dynamics, such as tail reconnection, is the total amount of open flux in the magnetosphere [*Badman et al.*, 2005]. Figure 10 shows the time history of the total amount of open flux in the polar cap, which is calculated by integrating the magnetic flux in the area inside the open-closed field line boundary identified by
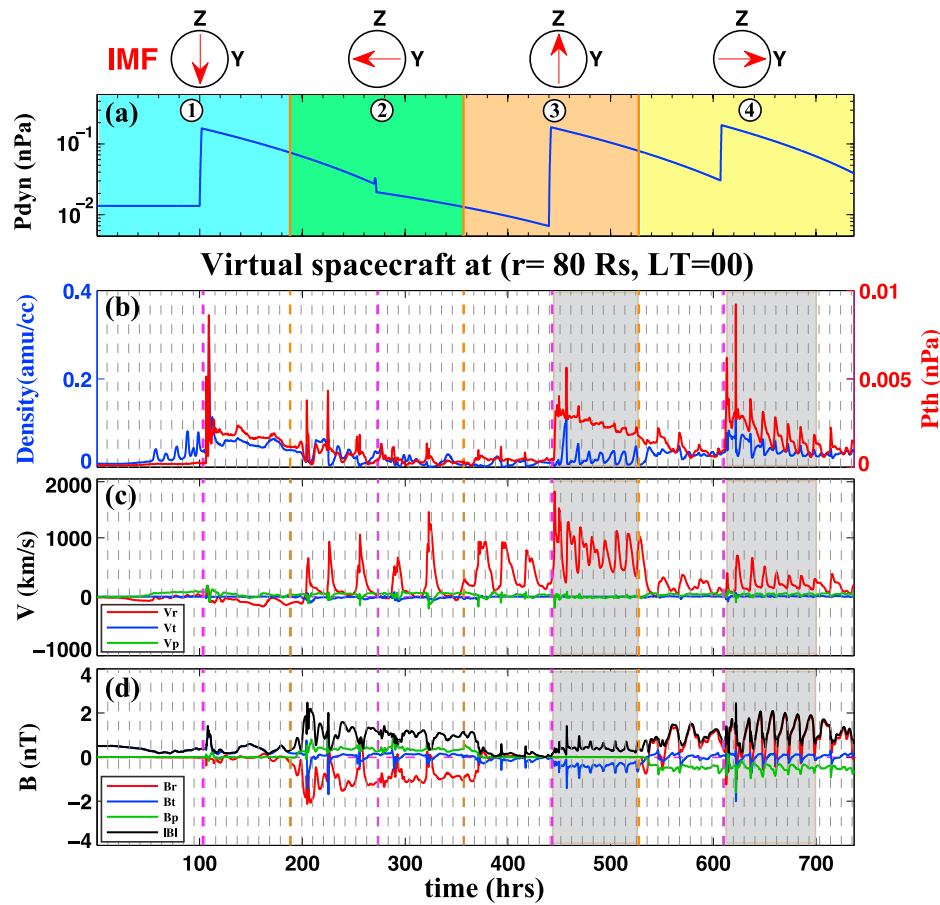
Figure 9. Modeled field and plasma parameters through the whole simulation interval as observed by a virtual spacecraft located at X = −80 R_S on the midnight meridian at the equator. (a) The upstream solar wind dynamic pressure and the IMF orientation. (b) Plasma density (in blue) and thermal pressure (in red), (c) the vector components (in spherical coordinates) of the flow velocity, and (d) the vector components (in spherical coordinates) and magnitude of the magnetic field. Consecutive dashed vertical lines are separated by one rotation period.

tracing 3D field lines in the simulation domain. Field lines with one end attached to the simulation inner boundary and the other reaching the simulation outer boundary are considered open field lines. It should be noted that if there were any X-lines outside our simulation domain whose downstream outer boundary is at X = −576 R_S, then the definition of open field lines used here may result in an overestimation of the total amount of open flux. In our model, we use a field strength of 20800 nT for the equatorial surface strength of Saturn's internal dipole rather than the Cassini value of 21084 nT [*Dougherty et al.*, 2005]. We note that this approximation only results in a very small difference (~1%) in the calculated total amount of open flux. During interval 1 when the IMF is southward, very little of the polar cap flux is open (~ several GWb), similar to the situation seen at Earth during periods of northward IMF. As the IMF rotates from southward to dawnward at the beginning of interval 2, the amount of open flux starts to increase as the result of dayside reconnection. During the rest of the simulation interval, with the IMF maintained in either the spiral or northward orientations (both favorable for dayside reconnection), the total amount of open flux in the polar cap remains between ~20 and ~35 GWb but exhibits some oscillatory variations

(quasi-periodic increases and decreases). The increases result from the accumulation of open flux produced by dayside reconnection with little reconnection occurring in the tail. The major decreases in the open flux are primarily associated with large-scale reconnection events in the tail, an association established by comparing the timings between each drop in the open flux and the reconnection/plasmoid signatures seen in the tail (e.g., Figure 9). We find that the amount of flux closed during individual reconnection events varies as the external solar wind conditions change. To better illustrate the results, we plot in Figure 11 the time between consecutive reconnection events and the change of open flux associated with each reconnection event as a function of the upstream solar wind dynamic pressure. While the repetition time of large-scale tail reconnection in general decreases with increasing dynamic pressure, consistent with the results shown in section 3.2.3, the amount of flux closed through each event shows no clear dependence on the upstream dynamic pressure.

[38] *Jackman et al.* [2011] estimated the amount of open flux closed through tail reconnection using observed magnetic field signatures in reconnection events combined with assumptions about the reconnection outflow speed and the
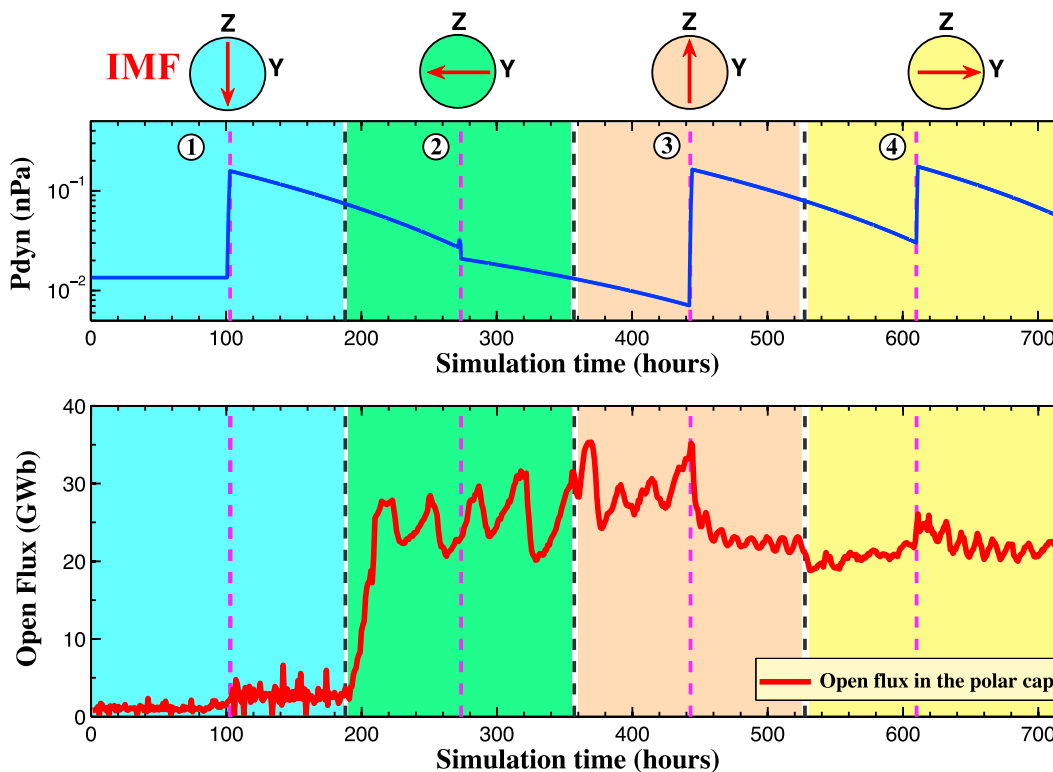
Figure 10. Time history of the total amount of open flux in the polar cap extracted from the simulation. (top) The upstream solar wind dynamic pressure and IMF orientation and (bottom) the total open flux in the simulation. Intervals with different IMF orientations are shaded with different colors. Vertical dashed lines indicate the arrival times of shocks (in magenta) and IMF rotations (in black).

length of tail X-line. Their analysis yielded an average amount of open flux of ~3 GWb. In our model, the amount of flux closure varies from case to case ranging from <1 GWb to ~10 GWb but the average amount of open flux closure is ~3.5 GWb, in good agreement with the estimate inferred from Cassini observations [*Jackman et al.*, 2011].

[39] As mentioned earlier, structures in the solar wind at Saturn's orbit are often dominated by CIRs, especially during the declining phase of the solar cycle [*Jackman et al.*, 2004]. The embedded shocks formed at the interface between the slow and fast solar wind in a CIR may initiate global responses in the magnetosphere [*Clarke et al.*, 2005; *Crary et al.*, 2005]. For example, it has been suggested that strong shock compression triggers large-scale tail reconnection and results in significant reconfiguration of the magnetosphere [*Cowley et al.*, 2005; *Bunce et al.*, 2005; *Jackman et al.*, 2010]. In interpreting the auroral observations obtained during the January 2004 Cassini-HST observing campaign, *Cowley et al.* [2005] proposed that, following a strong solar wind compression, magnetotail reconnection closes a significant fraction of the open flux in the tail lobes. We can examine the effects of shock compression on the global magnetosphere in our simulation by evaluating the associated changes in the open flux. A couple of shock events take place in our simulation. Here we focus on the cases of forward shocks that occur during intervals 3 and 4 when the magnetosphere is open. The shock around T = 442 h is a relatively strong shock while the one around T = 610 h is a relatively weak one as indicated by the magnitude of dynamic pressure

change across the shock. Correspondingly, we find no significant changes in the open flux during the weak shock event (T = 610 h). In contrast, the strong shock compression around T = 442 h produces a significant amount of open
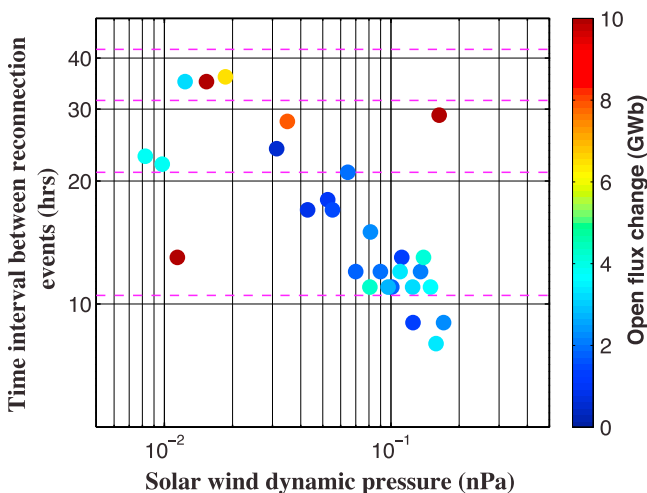

Figure 11. Scatterplot showing the repetition time of large-scale tail reconnection as a function of the upstream solar wind dynamic pressure (on a logarithmic scale). The scattered points are color coded according to the change of open flux during each reconnection event. Magenta horizontal lines show multiples of the planet rotation period.
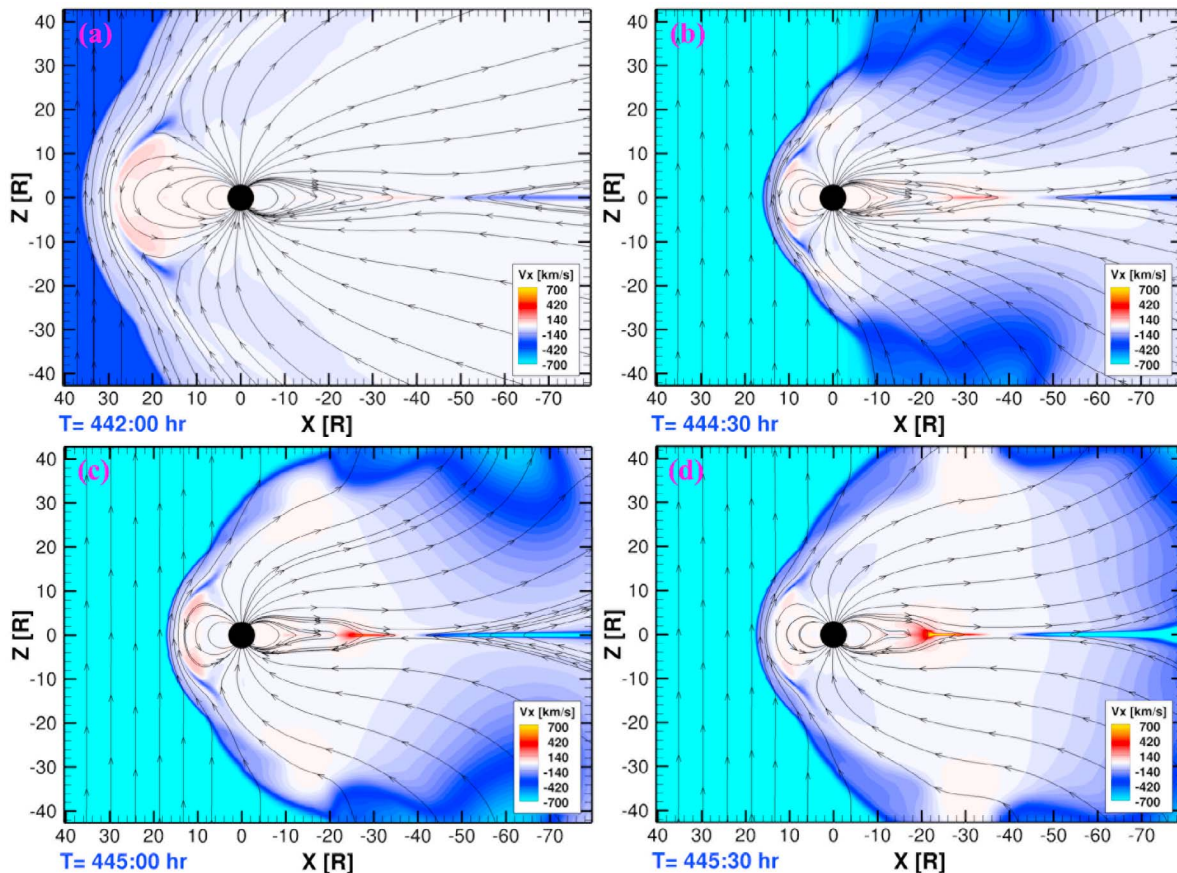
Figure 12. Magnetospheric configuration prior to and after the shock compression around T = 442 h. Color contours of V_x (km/s) and magnetic field lines in the XZ plane at Y = 0 (the noon-midnight meridian) are shown in each panel. (a) Model results at T = 442 h, prior to the shock arrival; (b–d) model results from subsequent times after the shock arrival.

flux closure over an interval of several hours. The amount of open flux closed during this event is ∼10 GWb, about 30% of the total amount of open flux in the polar cap prior to the shock event. To examine whether or not the shock compression induces tail reconnection thereby causing the reduction of open flux during this event, we show in Figure 12 simulation results from several time steps around the shock compression. Plotted in each panel of Figure 12 are color contours V_x and magnetic field lines in the noon-midnight meridian. The cyan color in the solar wind shows the high-speed stream behind the shock front. Figure 12a at T = 442:00 shows model results just prior to the shock arrival while Figures 12b–12d show the magnetospheric configuration at subsequent time steps. At T = 445:00 and T = 445:30, fast horizontal flows (both planetward and tailward) are seen near the center of the tail current sheet, indicative of tail reconnection. The sequence shown in Figure 12, therefore, clearly shows the association between the shock compression and tail reconnection. We suggest that the tail reconnection is triggered by the increase of magnetic pressure in the tail lobes resulting from the shock compression. To confirm this point, we compare the lobe field strength before and after the shock compression. Before the shock arrival, the tail lobe field strength at a radial distance of 25 Rs is about 4 nT. In comparison, when the magnetosphere

is compressed by the shock, the lobe field strength at the same distance increases by 50% to about 6 nT in response to the increase of the external pressure in the magnetosheath. Our model results, therefore, confirm the findings from previous observational studies that strong shock compression can induce reconnection in the tail leading to significant reduction of the open flux.

3.4. Global Magnetospheric Convection and the Release of Plasma From the Magnetosphere

[40] Global magnetospheric convection is driven by both internal and external sources of momentum. A snapshot from the simulation serves as an example that illustrates the interplay between the Vasyliūnas-cycle and the Dungey-cycle under conditions of strong solar wind driving. Figure 13 shows the global convection pattern extracted from a simulation time step (T = 482 h) when the solar wind dynamic pressure is relatively high after a shock compression and the IMF is northward, an orientation favorable for dayside reconnection. The background colors show contours of the horizontal flow velocity, V_x. Superimposed onto the V_x contours are colored balls showing intersections of selected closed field lines with the equatorial plane with the colors indicating their associated flux tube content (η) calculated according to $\eta = \int [\rho(s)/B(s)]ds$, where $\rho(s)$ is plasma mass
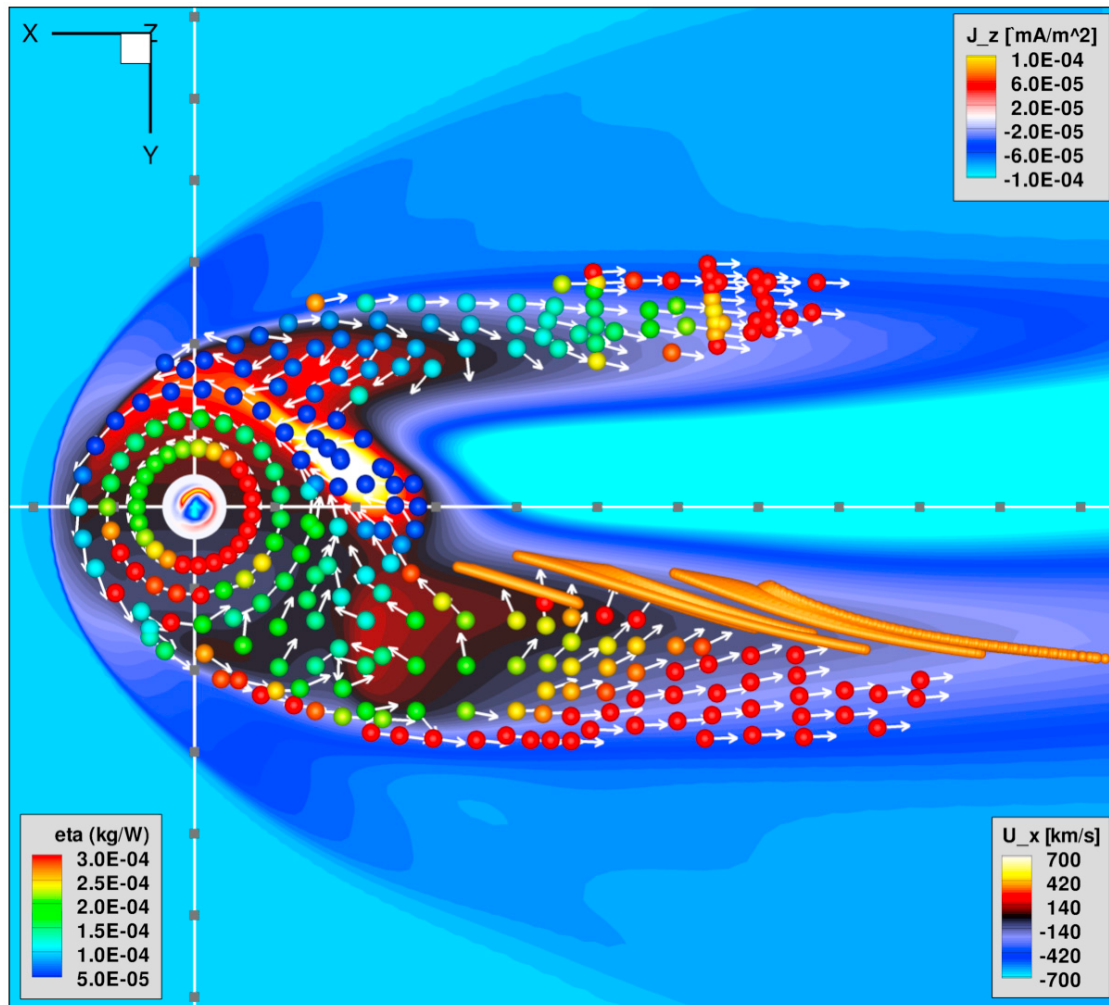
Figure 13. A snapshot of global convection and the distribution of flux tube content extracted from the simulation at a time (T = 482 h) when the IMF is northward. The background color contours represent the horizontal flow velocity (V_x) according to the bottom-right color bar and the color contours on a circular disk surrounding Saturn represent FACs intensity in the northern ionosphere (mapped to 4 R_S) according to the top-right color bar. The intersections of sampled closed field lines with the equatorial plane are plotted as balls color coded with their corresponding flux tube content (according to the bottom-left color bar). Also plotted are unit flow vectors of the closed field lines showing the direction of their motion. The orange traces show some representative field lines that form closed loops. Grey squares mark off every 10 R_S along the axes.

density, $B(s)$ is magnetic field strength and the integral is taken along a flux tube. As indicated by the flow vectors, plasmas in the inner and middle magnetosphere ($<15 \sim 20\,R_S$) move primarily in the corotation direction. In the outer magnetosphere ($>20\,R_S$), flow directions deviate significantly from the corotation direction. A prominent feature in the convection pattern is the presence of an X-line in the midnight to dawn sector across which fast flows reverse from tailward to planetward. As noted earlier, the high speeds indicate that the flows originate from reconnection between open field lines in the tail lobes. Therefore, this X-line is associated with the Dungey-cycle that involves open field line reconnection. On the tailward side of the X-line, those fast flows carry newly disconnected, interplanetary field lines down tail. On the planetward side, those fast flows occur on

depleted flux tubes with very low flux tube content (as indicated by the blue colors of the balls). They carry closed magnetic flux returning to the dayside via dawn in a region close to the dawnside magnetopause. Although the snapshot that we analyze in Figure 13 should not be thought of as representing a steady state (especially for varying solar wind conditions), it does reveal features that are typically present in the simulation. While the position and duration of the X-line changes as the external conditions change in our simulation, the Dungey-cycle X-line is always located primarily in the midnight-to-dawn sector. At slightly earlier local times (pre-midnight), the orange traces show some field lines in closed loops corresponding to small-scale plasmoids produced by reconnection on closed field lines (the Vasyliūnas-cycle); the trajectories of these closed loops

indicate the path of the plasmoid O-line. The magneto-spheric features associated with the Dungey-cycle and the Vasyliūnas-cycle seen in our simulation, such as the relative location of reconnection sites and the resulting convection pattern, are, in general, consistent with the predictions of the theoretical model proposed by *Cowley et al.* [2005].

[41] As the returning flux tubes rotate around noon, they gradually refill with planetary plasma. As they continue to rotate beyond the dusk sector, those now-full flux tubes are no longer confined by the magnetopause; they move farther from the planet and the associated field configurations become more and more stretched. As they continue to stream down tail, portions of those flux tubes carrying magnetospheric plasma eventually break off at large distances (beyond $\sim$100 R_S) and planetary plasma is lost from the magneto-sphere, probably through pinching-off of relatively small-scale plasmoids. Therefore the duskside magnetotail appears to be an important region from which planetary plasma is able to escape, a situation similar to that proposed by *Kivelson and Southwood* [2005] in describing the plasma circulation and associated dynamics in Jupiter's magnetosphere. In addition, we find that a second region containing full flux tubes moving in the tailward direction also exists in the mag-netotail near the dawnside flank [*Kivelson and Southwood*, 2005]. As plasma losses on the flanks of the magnetotail also contribute to the overall removal of magnetospheric plasma, it is of interest to assess the relative importance of loss through plasmoid release and loss through the flanks in removing plasma from the magnetosphere.

[42] As a first step, we calculate the total mass lost via large-scale plasmoids that cross the entire magnetotail. The properties of those large-scale plasmoids have been charac-terized for the plasmoid event presented in section 3.2.2. For this event, at a distance of $\sim$80 R_S downtail, the average mass density is $\sim$0.1 amu/cm^3 in a volume of length $\sim$80 R_S with an approximately circular cross-section of radius $\sim$10 R_S. Therefore, the total mass contained in the plasmoid is about 10^6 kg. During interval 2, a large-scale plasmoid of similar size is pinched off every $\sim$30 h. This implies that the average rate of mass transport rate by large-scale plasmoids through a surface at 80 R_S downtail is about $(10^6$ kg$)/(30$ h$) \approx 10$ kg/s. Thus the large plasmoids carry only about 10% of the total rate of mass input (85 kg/s used in the simulation) added by the plasma source in the inner magnetosphere.

[43] Another way of stating the result is to note that if all the mass were to be lost via large-scale plasmoids, then the repetition time would be $(10^6$ kg$)/(85$ kg/s$) \approx 3$ h, far shorter than the repetition time seen in the simulation, which is on average about 30 h except during strong compression events. During intervals in which the magnetosphere is significantly compressed, the plasmoids are much smaller and their mass content is much lower. We conclude that the recurrence time of large plasmoids is generally much longer than what would be required if large-scale plasmoid release were the primary process of removing plasma from the magnetosphere. It follows that other process(es) that facilitate plasma removal must be operating in the system. We propose that a large fraction of magnetospheric plasma is lost through the mag-netotail at the flanks, probably through pinching-off of rel-atively small-scale plasmoids rather than the large-scale plasmoids discussed in section 3.2.

[44] An alternative approach to estimating the mass loss rate is to evaluate the time history of the net mass flux through the YZ plane at a fixed downtail distance which we take to be X = -50 R_S. The result of this analysis is shown in Figure 14 (a positive value means the net flux is in the tailward direction), from which it can be seen that of order 60% of the required mass loss is accounted for. In obtaining the values plotted, it was necessary to distinguish magneto-spheric from magnetosheath plasma. The distinction was made using a crude criteria based on plasma beta (β). We first take the low-latitude portion of the contour line of a suitably chosen β-value ($\beta = 5$ in this analysis) as an approximation of the boundary at the flanks that separates the region containing magnetospheric plasma from that of magnetosheath plasma. The total mass loss rate is then cal-culated by integrating the mass flux over the area within the box, of which the boundaries in the $\hat{Y}$-direction are defined through the β criteria and the northern and southern boundaries are set as Z = $\pm15R_S$, respectively. It is likely that the criteria used underestimate the total mass loss rate both because of the approximations made in identifying the magnetospheric plasma (e.g., the fixed β threshold) and because some plasma may be lost through the flanks inside of X = -50 R_S. For example, during interval 1, most of the large-scale plasmoids escape the magnetosphere from the dawnside magnetopause and likely merge with the sheath flow before they reach 50 R_S in the tail. Nonetheless, we think during most of the simulation interval the approach provides a reasonably good estimate of the mass loss from the magnetosphere.

[45] In Figure 14, the high, short-duration peaks are associated with large-scale plasmoid releases. It is evident that even when large-scale plasmoid events are absent, the measured mass fluxes do not drop to the zero level but rather remain at finite values (indicated by the baseline of the curve). The baseline fit to the curve can then be considered approximately as the mass flux contributed by plasma losses through relatively continuous processes, e.g., small-scale plasmoids may pinch-off near the flanks and diffuse out into the magnetosheath.

[46] We have confirmed that the total mass contained in the individual sharp peaks in Figure 14 corresponds well to the mass carried in the large-scale plasmoids observed further down tail. If we again take the plasmoid event around T = 225 h as an example, the total mass contained in the plasmoid can be approximated as the area defined by the triangular area between the red and blue curves over a $\sim$20 h interval. As the height of the triangle is 30 kg/s, the total mass transported above the background level is $\sim$$10^6$ kg, consistent with the result previously obtained. On the other hand, the mass flux associated with plasma loss near the flanks is continuous with a typical transport rate of $\sim$50 kg/s. Thus we conclude from the simulation that plasma loss through large-scale plasmoid releases removes only a small fraction of the mass added by the internal plasma sources (Enceladus and its neutral cloud) and that a large fraction of the planetary plasma is lost through the flanks of the tail by processes probably involving small-scale plasmoids.

[47] Although our simulation is designed to represent Saturn's magnetosphere, a similar situation may exist at
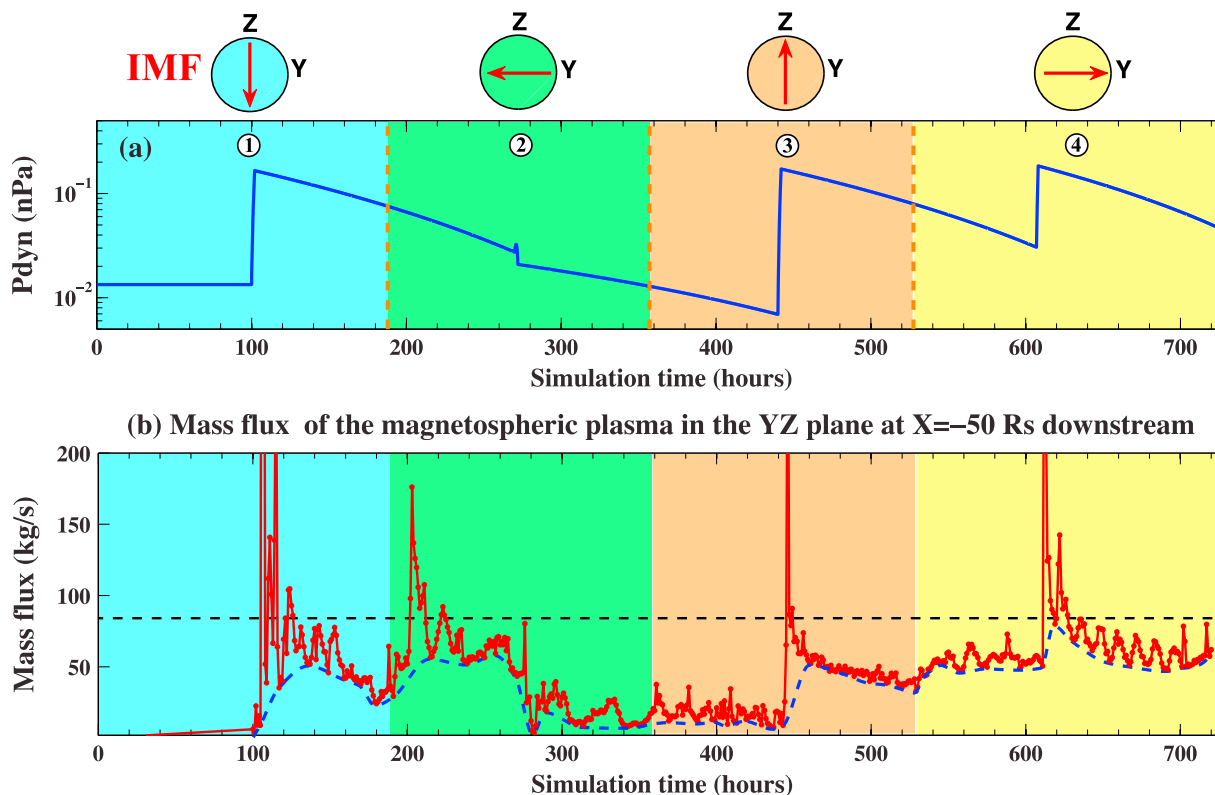
Figure 14. Time history of mass flux of the magnetospheric plasma lost down tail as measured in the YZ plane at X = −50 R_S. (a) The upstream solar wind dynamic pressure and IMF orientation are shown. Vertical lines indicate the times of IMF rotations. (b) The red curve shows the mass flux of plasma outflow measured at different simulation times and the blue trace shows a baseline fit to the red curve. The horizontal dashed line marks the total mass input rate of 85 kg/s used in the model.

Jupiter where Io and its plasma torus add plasma to the magnetosphere at a rate of about 500 kg/s [*Bagenal*, 2007]. In considering the role of plasmoid release in removing plasma from Jupiter's magnetosphere, *Bagenal* [2007] found that the plasma loss via large-scale plasmoids appears to carry away only a small fraction of the total mass added to the magnetosphere by Io and its plasma torus. They therefore concluded that plasma loss from the Jovian magnetosphere must occur principally via small-scale plasmoids and/or through diffusive processes near the flanks of the magnetotail.

4. Aspects of the Saturn System to be Incorporated in Future Simulation Runs

[48] In the simulation presented here, we have assumed that the solar wind flow is orthogonal to Saturn's rotation and dipole axes, a situation close to that near Saturn's equinox. However, Saturn's large obliquity (∼26.7°) results in an effective tilt between Saturn's rotational (and dipole) equator and the solar wind flow, which varies with season over Saturn's orbital period (∼29 years) ranging between −26.7° and +26.7°. Accordingly, seasonal variations in the magnetosphere arise both from asymmetric solar illumination of the atmosphere, and also from changes in the angle between the incident solar wind velocity and the dipole axis that produces global-scale changes of magnetospheric

configuration that have not been modeled in our simulation. One result of the varying attack angle of the solar wind is that the current sheet assumes a bowl-like shape as observed by *Arridge et al.* [2008]. In the inner magnetosphere, the observed current sheet lies close to the magnetic equator whereas, at larger distances (beyond ∼20 R_S on the night side), the current sheet is displaced away from the equator. The warped structure of the current sheet has important consequences for the geometry of tail reconnection and associated plasmoid structure. For example, a plasmoid, which presumably is formed near the center of the current sheet, would travel in the tail along a path displaced away from the nominal equator. Other seasonal effects include conductivity differences between the two ionospheres arising from asymmetric solar illumination, which may affect the magnetosphere/ionosphere coupling. Therefore, additional simulations taking into account these effects are needed in order to fully characterize seasonal variations in the global magnetospheric configuration and dynamics.

[49] One of the most unexpected aspects of Saturn's magnetosphere uncovered during the Cassini mission is the periodic modulation of various plasma and field phenomena in the magnetosphere and ionosphere. Cassini observations have revealed that properties of Saturn's magnetospheric plasma [e.g., *Paranicas et al.*, 2005; *Carbary et al.*, 2007; *Mitchell et al.*, 2009b; *Khurana et al.*, 2009; *Gurnett et al.*, 2007], magnetic field [e.g., *Espinosa et al.*, 2003; *Southwood*

and Kivelson, 2007; *Andrews et al.*, 2008] and radio emissions [e.g., *Kurth et al.*, 2007; *Gurnett et al.*, 2009; *Lamy*, 2012] vary at a ∼10.7 h period, close to that of planetary rotation with drifts of ∼1% per year. The source of the electromagnetic periodicities, however, is not understood. Although the periodicity has been accounted for in various ways (see a review by *Mitchell et al.* [2009a]), none has convincingly explained the observations. Recently, *Jia et al.* [2012] proposed that the upper atmosphere/ionosphere is a plausible source region for the periodicity. They carried out a global simulation in which they imposed vortical flows fixed in the high latitude thermosphere/ionosphere and demonstrated that the imposed flow vortex drives a variety of periodic phenomenon in the magnetosphere with features consistent with Cassini observations. In the study of *Jia et al.* [2012], the authors used a steady and non-reconnecting solar wind input (southward IMF) in order to focus on the effects of the vortex on the magnetosphere. Given the results presented in this paper that demonstrate the influence of the solar wind on the global configuration and magnetospheric dynamics, especially under conditions of strong solar wind driving, we intend to extend our modeling work by including an ionospheric flow vortex and driving the system with time-varying (rather than steady) solar wind input containing various types of disturbances, such as the ones investigated in this paper. We believe such an experiment will enable us to obtain a better understanding of the periodic phenomena and associated magnetospheric dynamics in Saturn's magnetosphere.

5. Summary and Conclusions

[50] We have investigated the solar wind interaction with Saturn's magnetosphere by using a global MHD simulation that self-consistently couples the ionosphere with the magnetosphere. As contrasted with previous global models, our new model adopts a high-resolution spherical grid that enables us to better resolve the large-scale magnetospheric currents responsible for the coupling between the magnetosphere and ionosphere. To characterize the response of the Kronian magnetosphere to the solar wind driving, we adopt an idealized time-varying solar wind input that includes features of CIRs typically seen at Saturn.

[51] Our global model driven by time-varying solar wind conditions allows us to examine the response of the magnetospheric boundaries to changes in external conditions. Our model results indicate that the magnetopause location, determined primarily by the balance between the internal and external pressures, is insensitive to the direction of the IMF. We have compared the modeled locations of the magnetopause and the bow shock with those predicted by empirical models constructed based on in-situ observations. The magnetopause locations in our MHD simulation show a good agreement with the predictions by the data-based model of *Kanani et al.* [2010] for various solar wind dynamic pressure and IMF conditions considered. The dependence of the magnetopause location on the solar wind dynamic pressure in our model confirms that Saturn's magnetopause is neither as rigid as the Earth's nor as compressible as Jupiter's. For the bow shock, we have compared our MHD model results with the predictions from the data-based model of *Masters et al.* [2008] that provides a convenient way to estimate the

shock location based on the upstream solar wind dynamic pressure. The comparison shows a good agreement for medium and high dynamic pressure conditions. However, the MHD-modeled bow shock locations under low (<∼0.02 nPa) dynamic pressure conditions are better predicted by an empirical model [e.g., *Farris and Russell*, 1994] that considers not only the properties of the incident solar wind but also the size of the magnetopause.

[52] In studying the dynamics of the magnetosphere, we have focused on large-scale reconnection and plasmoid formation in the magnetotail. Our model shows that the centrifugal acceleration associated with the planetary rotation leads to reconnection on mass-loaded closed flux tubes, forming plasmoids that carry planetary plasma away from the magnetosphere, an internal process inherent in a rotationally driven magnetosphere as proposed by *Vasyliūnas* [1983]. In addition to the Vasyliūnas-cycle, another type of reconnection process involving open field lines (referred to as the Dungey-cycle) is also seen in our simulation when the external conditions are favorable for dayside magnetopause reconnection. Under such circumstances, plasmoid formation in the tail also induces reconnection between open field lines from the tail lobes, producing global impacts on the magnetosphere. The Dungey-cycle reconnection typically results in fast flows and low densities in the outflows from the reconnection site. Tailward-moving flows carrying newly reconnected, interplanetary field lines accelerate the plasmoid ahead of them down the tail. Hot, tenuous plasma is carried inward in rapidly moving flux tubes returning from the tail reconnection site to the dayside. Such flux tubes may generate significant disturbances in the magnetosphere and the ionosphere, particularly on the dawn side, such as producing intense field-aligned currents that would be expected to cause aurora to brighten.

[53] We have also investigated how the properties of tail reconnection are affected by the external conditions. We find that the repetition time of large-scale tail reconnection varies as the external conditions change. In general, the recurrence rate tends to be higher as the solar wind dynamic pressure becomes higher. The amount of open flux closed through each tail reconnection event also varies from case to case and the average value in our model is ∼3.5 GWb, which is in a good agreement with the estimate inferred from Cassini observations of tail reconnection events [*Jackman et al.*, 2011].

[54] Our simulation allows us to examine the magnetospheric impacts of interplanetary shocks, typical structures embedded in the solar wind at Saturn. The model results show that a strong shock compression may trigger large-scale tail reconnection leading to significant reduction of open flux and reconfiguration of the magnetosphere, consistent with the picture proposed by *Cowley et al.* [2005] in interpreting auroral observations.

[55] We have discussed the global convection pattern resulting from the interplay between the Vasyliūnas-cycle and the Dungey-cycle. When only the Vasyliūnas-cycle is operating, such as during intervals of southward IMF, the associated X-line is found to form primarily in the midnight-to-dawn sector. When both processes are at work, the pure Vasyliūnas-cycle X-line is confined to a limited region in the pre-midnight sector while the Dungey-cycle X-line, albeit variable both in space and time, is seen primarily in the

midnight-to-dawn sector, adjacent to the Vasyliūnas-cycle X-line. We find such a pattern is, in general, consistent with the predictions from the theoretical model proposed by *Cowley et al.* [2005]. In addition, we have identified regions in the magnetotail near the flanks that contain flux tubes filled with magnetospheric plasma streaming down the tail. The breaking-off of those flux tubes (likely through small-scale plasmoid release) at large distances suggest these regions are important for releasing plasma from the magnetosphere, a situation similar to that proposed by *Kivelson and Southwood* [2005] in a Jovian context. We have assessed the relative importance of large-scale plasmoid release and losses through the magnetotail near the flanks in removing plasma from the magnetosphere. Our calculations show that the mass lost via large-scale plasmoid release appears to be only a small fraction (∼10%) of the total mass added by the internal plasma sources (Enceladus and its neutral cloud) and that a large fraction of the planetary plasma are lost through processes (e.g., small-scale plasmoids) near the flanks of the magnetotail, a situation that may also exist at Jupiter.

[57] Masaki Fujimoto thanks the reviewers for their assistance in evaluating the paper.

References

Achilleos, N., C. S. Arridge, C. Bertucci, C. M. Jackman, M. K. Dougherty, K. K. Khurana, and C. T. Russell (2008), Large-scale dynamics of Saturn's magnetopause: Observations by Cassini, *J. Geophys. Res.*, *113*, A11209, doi:10.1029/2008JA013265.

Andrews, D. J., E. J. Bunce, S. W. H. Cowley, M. K. Dougherty, G. Provan, and D. J. Southwood (2008), Planetary period oscillations in Saturn's magnetosphere: Phase relation of equatorial magnetic field oscillations and Saturn kilometric radiation modulation, *J. Geophys. Res.*, *113*, A09205, doi:10.1029/2007JA012937.

Arridge, C. S., N. Achilleos, M. K. Dougherty, K. K. Khurana, and C. T. Russell (2006), Modeling the size and shape of Saturn's magnetopause with variable dynamic pressure, *J. Geophys. Res.*, *111*, A11227, doi:10.1029/2005JA011574.

Arridge, C. S., K. K. Khurana, C. T. Russell, D. J. Southwood, N. Achilleos, M. K. Dougherty, A. J. Coates, and H. K. Leinweber (2008), Warping of Saturn's magnetospheric and magnetotail current sheets, *J. Geophys. Res.*, *113*, A08217, doi:10.1029/2007JA012963.

Atreya, S. K., T. M. Donahue, A. F. Nagy, J. H. Waite Jr., and J. C. McConnell (1984), Theory, measurements, and models of the upper atmosphere and ionosphere of Saturn, in *Saturn*, edited by T. Gehrels and M. S. Matthews, pp. 239–277, Univ. of Ariz. Press, Tucson.

Badman, S. V., and S. W. H. Cowley (2007), Significance of Dungey-cycle flows in Jupiter's and Saturn's magnetospheres, and their identification on closed equatorial field lines, *Ann. Geophys.*, *25*, 941–951, doi:10.5194/angeo-25-941-2007.

Badman, S. V., E. J. Bunce, J. T. Clarke, S. W. H. Cowley, J.-C. Gérard, D. Grodent, and S. E. Milan (2005), Open flux estimates in Saturn's magnetosphere during the January 2004 Cassini-HST campaign, and implications for reconnection rates, *J. Geophys. Res.*, *110*, A11216, doi:10.1029/2005JA011240.

Bagenal, F. (2007), The magnetosphere of Jupiter: Coupling the equator to the poles, *J. Atmos. Terr. Phys.*, *69*, 387–402, doi:10.1016/j.jastp.2006.08.012.

Bagenal, F., and P. A. Delamere (2011), Flow of mass and energy in the magnetospheres of Jupiter and Saturn, *J. Geophys. Res.*, *116*, A05209, doi:10.1029/2010JA016294.

Bunce, E. J., S. W. H. Cowley, and J. A. Wild (2003), Azimuthal magnetic fields in Saturn's magnetosphere: Effects associated with plasma sub-corotation and the magnetopause-tail current system, *Ann. Geophys.*, *21*, 1709–1722, doi:10.5194/angeo-21-1709-2003.

Bunce, E. J., S. W. H. Cowley, D. M. Wright, A. J. Coates, M. K. Dougherty, N. Krupp, W. S. Kurth, and A. M. Rymer (2005), In situ observations of a solar wind compression-induced hot plasma injection in Saturn's tail, *Geophys. Res. Lett.*, *32*, L20S04, doi:10.1029/2005GL022888.

Bunce, E. J., et al. (2008), Origin of Saturn's aurora: Simultaneous observations by Cassini and the Hubble Space Telescope, *J. Geophys. Res.*, *113*, A09209, doi:10.1029/2008JA013257.

Burger, M. H., E. C. Sittler, R. E. Johnson, H. T. Smith, O. J. Tucker, and V. I. Shematovich (2007), Understanding the escape of water from Enceladus, *J. Geophys. Res.*, *112*, A06219, doi:10.1029/2006JA012086.

Carbary, J. F., D. G. Mitchell, S. M. Krimigis, D. C. Hamilton, and N. Krupp (2007), Charged particle periodicities in Saturn's outer magnetosphere, *J. Geophys. Res.*, *112*, A06246, doi:10.1029/2007JA012351.

Cassidy, T. A., and R. E. Johnson (2010), Collisional spreading of Enceladus' neutral cloud, *Icarus*, *209*, 696–703, doi:10.1016/j.icarus.2010.04.010.

Cheng, A. F., and J. H. Waite (1988), Corotation lag of Saturn's magnetosphere: Global ionospheric conductivities revisited, *J. Geophys. Res.*, *93*, 4107–4109, doi:10.1029/JA093iA05p04107.

Clarke, J. T., et al. (2005), Morphological differences between Saturn's ultraviolet aurorae and those of Earth and Jupiter, *Nature*, *433*, 717–719, doi:10.1038/nature03331.

Connerney, J. E. P., M. H. Acuna, and N. F. Ness (1983), Currents in Saturn's magnetosphere, *J. Geophys. Res.*, *88*, 8779–8789, doi:10.1029/JA088iA11p08779.

Cowley, S., E. Bunce, and R. Prangé (2004), Saturn's polar ionospheric flows and their relation to the main auroral oval, *Ann. Geophys.*, *22*, 1379–1394, doi:10.5194/angeo-22-1379-2004.

Cowley, S. W. H., S. V. Badman, E. J. Bunce, J. T. Clarke, J. Gérard, D. Grodent, C. M. Jackman, S. E. Milan, and T. K. Yeoman (2005), Reconnection in a rotation-dominated magnetosphere and its relation to Saturn's auroral dynamics, *J. Geophys. Res.*, *110*, A02201, doi:10.1029/2004JA010796.

Cowley, S. W. H., C. S. Arridge, E. J. Bunce, J. T. Clarke, A. J. Coates, M. K. Dougherty, J. Gérard, D. Grodent, J. D. Nichols, and D. L. Talboys (2008), Auroral current systems in Saturn's magnetosphere: Comparison of theoretical models with Cassini and HST observations, *Ann. Geophys.*, *26*, 2613–2630, doi:10.5194/angeo-26-2613-2008.

Crary, F. J., et al. (2005), Solar wind dynamic pressure and electric field as the main factors controlling Saturn's aurorae, *Nature*, *433*, 720–722, doi:10.1038/nature03333.

Dougherty, M. K., et al. (2005), Cassini magnetometer observations during Saturn orbit insertion, *Science*, *307*, 1266–1270, doi:10.1126/science.1106098.

Espinosa, S. A., D. J. Southwood, and M. K. Dougherty (2003), How can Saturn impose its rotation period in a noncorotating magnetosphere?, *J. Geophys. Res.*, *108*(A2), 1086, doi:10.1029/2001JA005084.

Farris, M. H., and C. T. Russell (1994), Determining the standoff distance of the bow shock: Mach number dependence and use of models, *J. Geophys. Res.*, *99*, 17,681–17,689, doi:10.1029/94JA01020.

Fleshman, B. L., P. A. Delamere, and F. Bagenal (2010), A sensitivity study of the Enceladus torus, *J. Geophys. Res.*, *115*, E04007, doi:10.1029/2009JE003372.

Fukazawa, K., T. Ogino, and R. J. Walker (2007a), Magnetospheric convection at Saturn as a function of IMF B_Z, *Geophys. Res. Lett.*, *34*, L01105, doi:10.1029/2006GL028373.

Fukazawa, K., T. Ogino, and R. J. Walker (2007b), Vortex-associated reconnection for northward IMF in the Kronian magnetosphere, *Geophys. Res. Lett.*, *34*, L23201, doi:10.1029/2007GL031784.

Gombosi, T. I., D. L. De Zeeuw, C. P. T. Groth, and K. G. Powell (2000), Magnetospheric configuration for Parker-Spiral IMF conditions: Results of a 3D AMR MHD simulation, *Adv. Space Res.*, *26*, 139–149, doi:10.1016/S0273-1177(99)01040-6.

Gombosi, T. I., G. Tóth, D. L. De Zeeuw, K. C. Hansen, K. Kabin, and K. G. Powell (2002), Semi-relativistic magnetohydrodynamics and physics-based convergence acceleration, *J. Comput. Phys.*, *177*, 176–205, doi:10.1006/jcph.2002.7009.

Gombosi, T. I., et al. (2004), Solution-adaptive magnetohydrodynamics for space plasmas: Sun-to-Earth simulations, *Comput. Sci. Eng.*, *6*(2), 14–35, doi:10.1109/MCISE.2004.1267603.

Gurnett, D. A., A. M. Persoon, W. S. Kurth, J. B. Groene, T. F. Averkamp, M. K. Dougherty, and D. J. Southwood (2007), The variable rotation period of the inner region of Saturn's plasma disk, *Science*, *316*, 442–445, doi:10.1126/science.1138562.

Gurnett, D. A., A. Lecacheux, W. S. Kurth, A. M. Persoon, J. B. Groene, L. Lamy, P. Zarka, and J. F. Carbary (2009), Discovery of a north–south asymmetry in Saturn's radio rotation period, *Geophys. Res. Lett.*, *36*, L16102, doi:10.1029/2009GL039621.

Hansen, C. J., L. Esposito, A. I. F. Stewart, J. Colwell, A. Hendrix, W. Pryor, D. Shemansky, and R. West (2006), Enceladus' water vapor plume, *Science*, *311*, 1422–1425, doi:10.1126/science.1121254.

Hansen, K. C., T. I. Gombosi, D. L. Dezeeuw, C. P. T. Groth, and K. G. Powell (2000), A 3D global MHD simulation of Saturn's magnetosphere, *Adv. Space Res.*, *26*, 1681–1690, doi:10.1016/S0273-1177(00)00078-8.

Hansen, K. C., A. J. Ridley, G. B. Hospodarsky, N. Achilleos, M. K. Dougherty, T. I. Gombosi, and G. Tóth (2005), Global MHD simulations of Saturn's magnetosphere at the time of Cassini approach, *Geophys. Res. Lett.*, *32*, L20S06, doi:10.1029/2005GL022835.

Hendricks, S., F. M. Neubauer, M. K. Dougherty, N. Achilleos, and C. T. Russell (2005), Variability in Saturn's bow shock and magnetopause from Pioneer and Voyager: Probabilistic predictions and initial observations by Cassini, *Geophys. Res. Lett.*, *32*, L20S08, doi:10.1029/2005GL022569.

Hill, T. W., et al. (2008), Plasmoids in Saturn's magnetotail, *J. Geophys. Res.*, *113*, A01214, doi:10.1029/2007JA012626.

Hu, Y. Q., X. C. Guo, and C. Wang (2007), On the ionospheric and reconnection potentials of the earth: Results from global MHD simulations, *J. Geophys. Res.*, *112*, A07215, doi:10.1029/2006JA012145.

Huddleston, D. E., C. T. Russell, M. G. Kivelson, K. K. Khurana, and L. Bennett (1998), Location and shape of the Jovian magnetopause and bow shock, *J. Geophys. Res.*, *103*, 20,075–20,082, doi:10.1029/98JE00394.

Jackman, C. M., N. Achilleos, E. J. Bunce, S. W. H. Cowley, M. K. Dougherty, G. H. Jones, S. E. Milan, and E. J. Smith (2004), Interplanetary magnetic field at ~9 AU during the declining phase of the solar cycle and its implications for Saturn's magnetospheric dynamics, *J. Geophys. Res.*, *109*, A11203, doi:10.1029/2004JA010614.

Jackman, C. M., C. T. Russell, D. J. Southwood, C. S. Arridge, N. Achilleos, and M. K. Dougherty (2007), Strong rapid dipolarizations in Saturn's magnetotail: In situ evidence of reconnection, *Geophys. Res. Lett.*, *34*, L11203, doi:10.1029/2007GL029764.

Jackman, C. M., R. J. Forsyth, and M. K. Dougherty (2008), The overall configuration of the interplanetary magnetic field upstream of Saturn as revealed by Cassini observations, *J. Geophys. Res.*, *113*, A08114, doi:10.1029/2008JA013083.

Jackman, C. M., C. S. Arridge, J. A. Slavin, S. E. Milan, L. Lamy, M. K. Dougherty, and A. J. Coates (2010), In situ observations of the effect of a solar wind compression on Saturn's magnetotail, *J. Geophys. Res.*, *115*, A10240, doi:10.1029/2010JA015312.

Jackman, C. M., J. A. Slavin, and S. W. H. Cowley (2011), Cassini observations of plasmoid structure and dynamics: Implications for the role of magnetic reconnection in magnetospheric circulation at Saturn, *J. Geophys. Res.*, *116*, A10212, doi:10.1029/2011JA016682.

Jia, X., M. G. Kivelson, and T. I. Gombosi (2012), Driving Saturn's magnetospheric periodicities from the upper atmosphere/ionosphere, *J. Geophys. Res.*, *117*, A04215, doi:10.1029/2011JA017367.

Jurac, S., and J. D. Richardson (2005), A self-consistent model of plasma and neutrals at Saturn: Neutral cloud morphology, *J. Geophys. Res.*, *110*, A09220, doi:10.1029/2004JA010635.

Kanani, S. J., et al. (2010), A new form of Saturn's magnetopause using a dynamic pressure balance model, based on in situ, multi-instrument Cassini measurements, *J. Geophys. Res.*, *115*, A06207, doi:10.1029/2009JA014262.

Khurana, K. K., D. G. Mitchell, C. S. Arridge, M. K. Dougherty, C. T. Russell, C. Paranicas, N. Krupp, and A. J. Coates (2009), Sources of rotational signals in Saturn's magnetosphere, *J. Geophys. Res.*, *114*, A02211, doi:10.1029/2008JA013312.

Kidder, A., R. M. Winglee, and E. M. Harnett (2009), Regulation of the centrifugal interchange cycle in Saturn's inner magnetosphere, *J. Geophys. Res.*, *114*, A02205, doi:10.1029/2008JA013100.

Kivelson, M. G., and D. J. Southwood (2005), Dynamical consequences of two modes of centrifugal instability in Jupiter's outer magnetosphere, *J. Geophys. Res.*, *110*, A12209, doi:10.1029/2005JA011176.

Kurth, W. S., A. Lecacheux, T. F. Averkamp, J. B. Groene, and D. A. Gurnett (2007), A Saturnian longitude system based on a variable kilometric radiation period, *Geophys. Res. Lett.*, *34*, L02201, doi:10.1029/2006GL028336.

Lamy, L. (2012), Variability of southern and northern periodicities of Saturn kilometric radiation, in *Planetary Radio Emissions VII*, pp. 38–50, Austrian Acad. Sci. Press, Vienna.

Lyon, J. G., J. A. Fedder, and C. M. Mobarry (2004), The Lyon-Fedder-Mobarry (LFM) global MHD magnetospheric simulation code, *J. Atmos. Sol. Terr. Phys.*, *66*, 1333–1350.

Masters, A., N. Achilleos, M. K. Dougherty, J. A. Slavin, G. B. Hospodarsky, C. S. Arridge, and A. J. Coates (2008), An empirical model of Saturn's bow shock: Cassini observations of shock location and shape, *J. Geophys. Res.*, *113*, A10210, doi:10.1029/2008JA013276.

Masters, A., M. F. Thomsen, S. V. Badman, C. S. Arridge, D. T. Young, A. J. Coates, and M. K. Dougherty (2011), Supercorotating return flow from reconnection in Saturn's magnetotail, *Geophys. Res. Lett.*, *38*, L03103, doi:10.1029/2010GL046149.

Mitchell, D. G., J. F. Carbary, S. W. H. Cowley, T. W. Hill, and P. Zarka (2009a), The dynamics of Saturn's magnetosphere, in *Saturn from Cassini-Huygens*, edited by M. K. Dougherty, L. W. Esposito, and S. M. Krimigis, pp. 257–279, Springer, New York.

Mitchell, D. G., et al. (2009b), Recurrent energization of plasma in the midnight-to-dawn quadrant of Saturn's magnetosphere, and its relationship to auroral UV and radio emissions, *Planet. Space Sci.*, *57*, 1732–1742, doi:10.1016/j.pss.2009.04.002.

Moore, L., I. Mueller-Wodarg, M. Galand, A. Kliore, and M. Mendillo (2010), Latitudinal variations in Saturn's ionosphere: Cassini measurements and model comparisons, *J. Geophys. Res.*, *115*, A11317, doi:10.1029/2010JA015692.

Paranicas, C., D. G. Mitchell, E. C. Roelof, P. C. Brandt, D. J. Williams, S. M. Krimigis, and B. H. Mauk (2005), Periodic intensity variations in global ENA images of Saturn, *Geophys. Res. Lett.*, *32*, L21101, doi:10.1029/2005GL023656.

Powell, K. G., P. L. Roe, T. J. Linde, T. I. Gombosi, and D. L. D. Zeeuw (1999), A solution-adaptive upwind scheme for ideal magnetohydrodynamics, *J. Comput. Phys.*, *154*, 284–309.

Raeder, J., J. Berchem, and M. Ashour-Abdalla (1998), The Geospace Environment Modeling grand challenge: Results from a Global Geospace Circulation Model, *J. Geophys. Res.*, *103*(A7), 14,787–14,797.

Richardson, I. G., S. W. H. Cowley, E. W. Hones Jr., and S. J. Bame (1987), Plasmoid-associated energetic ion bursts in the deep geomagnetic tail: Properties of plasmoids and the postplasmoid plasma sheet, *J. Geophys. Res.*, *92*, 9997–10,013, doi:10.1029/JA092iA09p09997.

Richardson, J. D., A. Eviatar, M. A. McGrath, and V. M. Vasyliūnas (1998), OH in Saturn's magnetosphere: Observations and implications, *J. Geophys. Res.*, *103*, 20,245–20,256, doi:10.1029/98JE01127.

Ridley, A., T. Gombosi, and D. Dezeeuw (2004), Ionospheric control of the magnetosphere: Conductance, *Ann. Geophys.*, *22*, 567–584.

Shue, J., J. K. Chao, H. C. Fu, C. T. Russell, P. Song, K. K. Khurana, and H. J. Singer (1997), A new functional form to study the solar wind control of the magnetopause size and shape, *J. Geophys. Res.*, *102*, 9497–9512, doi:10.1029/97JA00196.

Sibeck, D. G., R. E. Lopez, and E. C. Roelof (1991), Solar wind control of the magnetopause shape, location, and motion, *J. Geophys. Res.*, *96*, 5489–5495, doi:10.1029/90JA02464.

Slavin, J. A., E. J. Smith, J. R. Spreiter, and S. S. Stahara (1985), Solar wind flow about the outer planets: Gas dynamic modeling of the Jupiter and Saturn bow shocks, *J. Geophys. Res.*, *90*, 6275–6286, doi:10.1029/JA090iA07p06275.

Smith, H. T., R. E. Johnson, M. E. Perry, D. G. Mitchell, R. L. McNutt, and D. T. Young (2010), Enceladus plume variability and the neutral gas densities in Saturn's magnetosphere, *J. Geophys. Res.*, *115*, A10252, doi:10.1029/2009JA015184.

Southwood, D. J., and M. G. Kivelson (2007), Saturnian magnetospheric dynamics: Elucidation of a camshaft model, *J. Geophys. Res.*, *112*, A12222, doi:10.1029/2007JA012254.

Spreiter, J. R., A. L. Summers, and A. Y. Alksne (1966), Hydromagnetic flow around the magnetosphere, *Planet. Space Sci.*, *14*, 223–250, doi:10.1016/0032-0633(66)90124-3.

Tóth, G., et al. (2005), Space weather modeling framework: A new tool for the space science community, *J. Geophys. Res.*, *110*, A12226, doi:10.1029/2005JA011126.

Tóth, G., et al. (2012), Adaptive numerical algorithms in space weather modeling, *J. Comput. Phys.*, *231*, 870–903, doi:10.1016/j.jcp.2011.02.006.

Vasyliūnas, V. M. (1983), Plasma distribution and flow, in *Physics of the Jovian Magnetosphere*, edited by A. J. Dessler, pp. 395–453, Cambridge Univ. Press, New York.

Went, D. R., G. B. Hospodarsky, A. Masters, K. C. Hansen, and M. K. Dougherty (2011), A new semiempirical model of Saturn's bow shock based on propagated solar wind parameters, *J. Geophys. Res.*, *116*, A07202, doi:10.1029/2010JA016349.

Zieger, B., and K. C. Hansen (2008), Statistical validation of a solar wind propagation model from 1 to 10 AU, *J. Geophys. Res.*, *113*, A08107, doi:10.1029/2008JA013046.

Zieger, B., K. C. Hansen, T. I. Gombosi, and D. L. DeZeeuw (2010), Periodic plasma escape from the mass-loaded Kronian magnetosphere, *J. Geophys. Res.*, *115*, A08208, doi:10.1029/2009JA014951.